Electronic Supplementary Information

Carbonization/Interfacial Assembly-Driven Electroplating Approach for Water-Splitting Textile Electrodes with Remarkably Low Overpotentials and High Operational Stability†

Jeongmin Mo,‡[a] Younji Ko,‡[a] Young Soo Yun,[b] June Huh,[a] and Jinhan Cho*[a,b]

[a] Department of Chemical and Biological Engineering, Korea University, 145 Anam-ro, Seongbuk-gu, Seoul 02841, Republic of Korea

[b] KU-KIST Graduate School of Converging Science and Technology, Korea University, 145 Anam-ro, Seongbuk-gu, Seoul 02841, Republic of Korea

‡These authors contributed equally to this work.

* Address correspondence to jinhan71@korea.ac.kr

† Electronic supplementary information (ESI) available. See DOI:

Experimental Section

Materials

All chemical reagents were purchased from Sigma−Aldrich and used without further purification. Silk textile was purchased from Coasilk (Republic of Korea), and Ni foam was purchased from Goodfellow Cambridge Ltd. (United Kingdom).

Preparation of the CST

The silk textile was first washed with deionized water and dried in an oven. It was then carbonized by heating to 950 °C at a rate of 3 °C min^{-1} and holding for 3 h in a furnace under a flow of nitrogen gas. After carbonization, the resulting CST was naturally cooled to room temperature.

Preparation of the COOH–CST and NH_2–CST

The CST was first oxidized by strong acid treatment with H_2SO_4/HNO_3 at 70 °C for 2 h to form COOH–CST. After treatment, COOH–CST was washed with deionized water and dried in an oven. Then, COOH–CST was immersed in a tris(2-aminoethyl)amine (TREN, 5 mg mL^{-1} dispersed in ethanol) solution for 3 h to prepare NH_2–CST.

Preparation of the EP Ni–CST

The as-prepared NH_2–CST was immersed in a Watt bath (240 g L^{-1} $NiSO_4$, 45 g L^{-1} $NiCl_2$ and 30 g L^{-1} H_3BO_3).[S1] NH_2–CST served as the cathode, and a nickel plate was used as the anode. Ni electroplating was performed at a current density of 360 mA cm^{-2} for 5 min using a power supply. Then, the electroplated sample was washed in deionized water and dried at room temperature (Ni loading amount: 40.6 mg cm^{-1}).

Preparation of the CR Ni–CST

Electroless (EL) Ni was deposited on NH_2–CST according to a reported procedure.[S2] NH_2–CST was first immersed in a sensitizing solution (0.05 M $SnCl_2 \cdot 2H_2O$ and 0.15 M HCl) and a $PdCl_2$ solution (0.6 mM $PdCl_2$ and 0.03 M HCl) and washed three times with deionized water. Then, 45 g L^{-1} $NiSO_4 \cdot 6H_2O$, 240 g L^{-1} $NaH_2PO_2 \cdot H_2O$, 30 g L^{-1} $NaC_6H_5O_7 \cdot 2H_2O$ and 50 g L^{-1} NH_4Cl were mixed together at room temperature and adjusted to pH 9 using NH_4OH. After increasing the temperature of the solution to 80 °C, the NH_2–CST substrate was immersed in the above mixture, and the mixture was stirred for 30 min. After the reaction, the sample was repeatedly washed with deionized water and dried at room temperature.

Preparation of the EP NiFeCo–CST

A NiFeCo layer was deposited on the prepared EP Ni–CST electrode from an aqueous electrolyte bath containing 3 mM $Ni(NO_3)_2 \cdot 6H_2O$, 3 mM $Fe(NO_3)_3 \cdot 9H_2O$ and 3 mM $Co(NO_3)_3 \cdot 6H_2O$. The one-step NiFeCo electroplating process was performed at a current density of 30 mA cm^{-2} for 10 min using a power supply. The EP Ni–CST was used as the cathode, and a nickel plate was used as the anode. After electrodeposition, the coated electrode was washed three times with deionized water and dried (NiFeCo loading amount: 2 mg cm^{-1}).

Preparation of the hydrothermal NiFeCo–CST

Hydrothermal deposition of NiFeCo on EP Ni-CST was conducted according to the reported procedure with a slight modification.[S3] Specifically, 4 mmol $Ni(NO_3)_2 \cdot 6H_2O$, 0.45 mmol $Fe(NO_3)_3 \cdot 9H_2O$, 0.45 mmol $Co(NO_3)_3 \cdot 6H_2O$, 20 mmol urea and 8 mmol NH_4F were dissolved in 80 mL of deionized water with magnetic stirring. Then, the obtained solution was transferred into a 100 mL Teflon-lined stainless-steel autoclave, and the cleaned EP Ni–CST was immersed into the solution. The autoclave was sealed and maintained at 120 °C for 3 h, and then the electrode was washed with deionized water and dried at 60 °C for 12 h.

Preparation of the EP NiFe–CST

A NiFe layer was deposited on the prepared EP Ni–CST electrode from an aqueous electrolyte bath containing 3 mM $Ni(NO_3)_2 \cdot 6H_2O$ and 3 mM $Fe(NO_3)_3 \cdot 9H_2O$. The one-step NiFe electroplating process was performed at a current density of 30 mA cm^{-2} for 10 min using a power supply. The EP Ni–CST was used as the cathode, and a nickel plate was used as the anode. After electrodeposition, the electrode was washed three times with deionized water and dried.

Preparation of the Pt/C electrodes

Pt/C electrodes were prepared by dispersing 1 mg of Pt/C (20 wt.% Pt on Vulcan XC-72) in 300 μL of an EtOH solution containing 10.5 μL of 5 wt.% Nafion.[S4] This resulting catalyst ink solution was deposited onto the CST or commercial Ni foam (0.5 × 0.5 cm^2) and then dried at room temperature.

Preparation of the IrO_2 electrodes

IrO_2 electrodes were prepared by dispersing 1 mg of IrO_2 in 300 μL of an EtOH solution with 10.5 μL of 5 wt.% Nafion.[S4] This IrO_2 catalyst ink solution was loaded onto the CST or commercial Ni foam (0.5 × 0.5 cm^2) in the same manner as the Pt/C electrode described above and then dried at room temperature.

Characterization

Raman spectroscopy was performed using a Horiba Jobin Yvon instrument. Water contact angles were determined by means of a Phoenix 300 instrument (S.E.O. Co., Ltd.). The crystallinities of the CST, EP Ni–CST, CR Ni–CST, and hydrothermal NiFeCo–CST surfaces were analyzed by X-ray diffraction (XRD), which was performed on a SmartLab instrument (Rigaku) with a Cu Kα radiation source. All the HR-TEM and the EDX mapping images were obtained using a FEI Titan Themi-3 Double Cs & Mono TEM equipped with the Chemi-STEM technology. The X-ray photoelectron spectroscopy (XPS) results of the electrodes were obtained using an XPS instrument (X-TOOL, ULVAC-PHI) with an Al Kα radiation source. All of the XPS spectra were corrected by calibrating

all peaks to the major C-C/C-H binding energy. The Fourier transform infrared (FTIR) spectroscopy results of CST, COOH–CST, and NH_2–CST were obtained with a Cary 600 spectrometer (Agilent Technology) operated at a 4 cm^{-1} resolution in attenuated total reflectance (ATR) mode, and the obtained data were plotted by means of spectral analysis software (OMNIC, Nicolet). Scanning electron microscopy (SEM) and energy-dispersive X-ray spectroscopy (EDX) images were obtained via field-emission SEM (FE-SEM) (Quanta 250 FEG, FEI). The Brunauer–Emmett–Teller (BET) specific surface areas of the electrodes were measured via N_2 (99.999%) adsorption at 77 K (Autosorb-iQ & Quadrasorb SI).

Electrochemical characterization

All electrochemical measurements, including the polarization curves, cyclic voltammetry curves, and electrochemical impedance spectroscopy (EIS) measurements, were conducted with an Ivium-n-Stat electrochemical workstation (Ivium Technologies). For measurements in the three-electrode cell system, a Pt mesh and a reversible hydrogen electrode (RHE) were used as the counter and reference electrodes, respectively, and the electrolyte was 1 M KOH (pH = 14). The OER and HER catalytic activities were measured by linear sweep voltammetry at scan rates of 2 mV s^{-1} with iR compensation. All reported current densities were based on the geometric surface area of the electrodes. The EIS measurements were performed with a biased working electrode at frequencies from 100 kHz to 0.01 Hz and potentials of 1.5 V (vs. RHE) for the OER and −0.1 V (vs. RHE) for the HER. In this case, the semicircle diameter indicates the charge transfer resistance (R_{ct}), which can be used to evaluate the charge transfer kinetics on the surface of the electrode. The starting point on the *x*-axis for the semicircle represents the series resistance (R_s), which is the sum of the ionic resistance of the electrolyte, the intrinsic resistance of the active material and the contact resistance at the active material/current collector interface.

Inductively coupled plasma mass spectrometry (ICP-MS, Agilent Technologies 7700) was performed to detect the amount of Ni ions dissolved in the electrolyte after the HER and the amounts of Ni, Fe, and Co ions dissolved in the electrolyte after the OER.

The Faradaic efficiency of water splitting was measured by the eudiometry method in an experimental setup. The working electrode was fixed on the inside of an inverted burette filled with electrolyte. All the metal wires connecting the working electrode were coated with insulating epoxy to prevent charge loss from the side reactions. The evolved gases were directly collected in the headspace of the inverted burette, and the corresponding gas volume was determined by the displacement of the vertical water column. Based on this method, the Faradaic efficiency was calculated by comparing the amount of evolved gas with the theoretical amount of gas, which was calculated by the charge passed through the electrode:

$$Faradaic\ efficiency\ (H_2) = \frac{V_{experiment}}{V_{theoretical}} = \frac{V_{experiment}}{\frac{2}{4} \times \frac{Q}{F} \times V_m} \quad (1)$$

$$Faradaic\ efficiency\ (O_2) = \frac{V_{experiment}}{V_{theoretical}} = \frac{V_{experiment}}{\frac{1}{4} \times \frac{Q}{F} \times V_m} \quad (2)$$

where F is the Faraday constant (96,485 C mol^{-1}), Q is the summation of the charge passed through the electrodes, the number 4 represents 4 moles of electrons per mole of H_2O, the number 2 represents 2 moles of H_2 per mole of H_2O, the number 1 represents 1 mole of O_2 per mole of H_2O and V_m is the molar volume of gas (24.5 L mol^{-1}, 298 K, 101 kPa).[S5]

DFT calculation

Spin-polarized DFT calculations were performed to theoretically compare the catalytic efficiency of three different kinds of OER electrode system (NiOOH, NiFeOOH, and NiFeCoOOH). All DFT computations were based on plane wave and PBE-GGA functional with ultrasoft pseudopotential

using CASTEP.[S6] The Hubbard approach was employed by the effective U-J terms having 5.5 eV, 3.3 eV, and 3.3 eV for Ni, Fe, and Co, respectively, taking into account errors from Coulombic repulsion between the electrons in the d-shell.[S7-S11] The model for NiOOH catalytic surfaces were prepared from β-NiOOH bulk crystal cleaved at $(01\bar{1}5)$ plane, a higher Miller-index surface, which was considered to be catalytically more active because the transition metal atoms are not fully coordinated.[S12,S13] The Fe- and FeCo-doped NiOOH catalytic surfaces were then prepared by replacing 4 Ni atoms (out of the total 10 Ni atoms in the model β-NiOOH$(01\bar{1}5)$ surface) to 4 Fe atoms for the model NiFeOOH, surface, and to 2 Fe and 2 Ni atoms for the model NiFeCoOOH, surface (**Fig. S22 (a)-(c)**) where Fe atom on the topmost layer for NiFeOOH, and NiFeCoOOH was assumed to be active site for OER.[S14,S15] In addition, a 13 Å-thick vacuum layer was introduced in each of catalytic surfaces to prevent the interaction between periodic images of neighboring supercells. For these prepared slabs, 3×3×1 Monkhorst-Pack k-point meshes were used to sample the Brillouin-zone with the convergence of energy within 0.0015 eV. Broyden-Fletcher-Goldfarb-Shanno algorithm were also employed for geometry optimization with the convergence criteria of the maximal force on each atom less than 0.025 eV/Å. The Gibbs free energy changes of each step of OER cycle under alkaline condition were computed according to **ref. S16**.[S16]

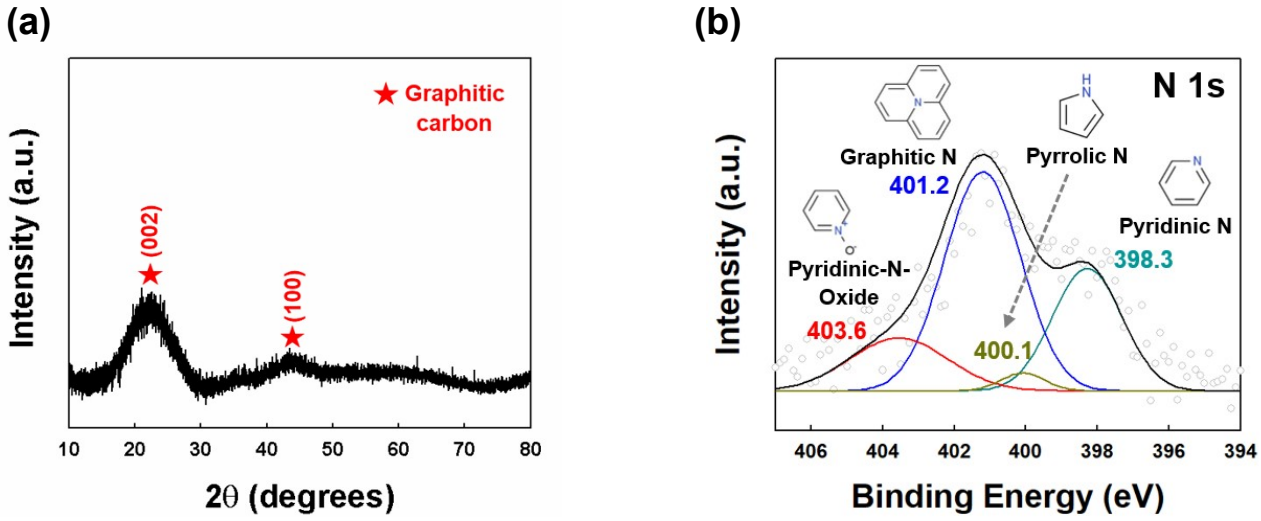

Fig. S1. (a) XRD patterns and (b) XPS spectra of N 1s for CST. [S17,S18]

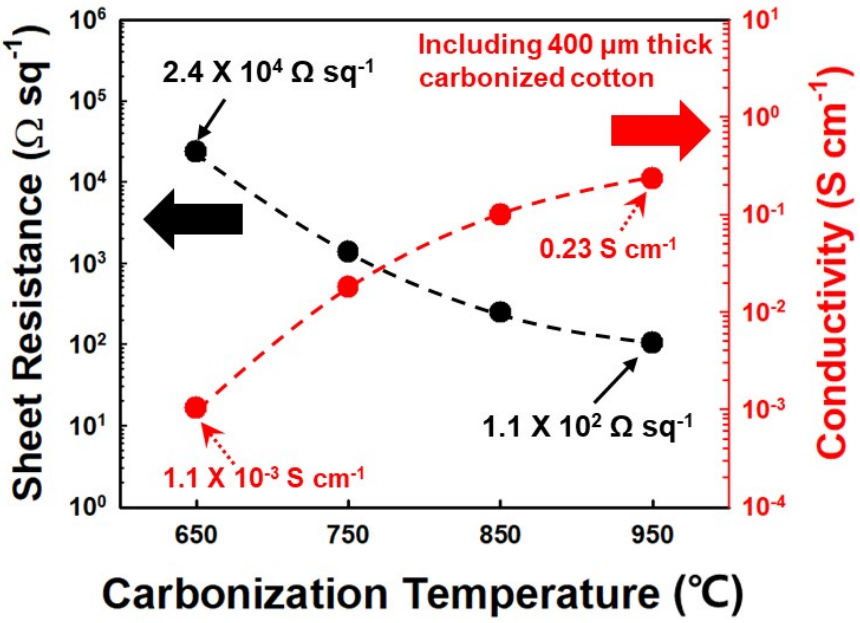

Fig. S2. Electrical properties of carbonized cotton textile with increasing carbonization temperature.

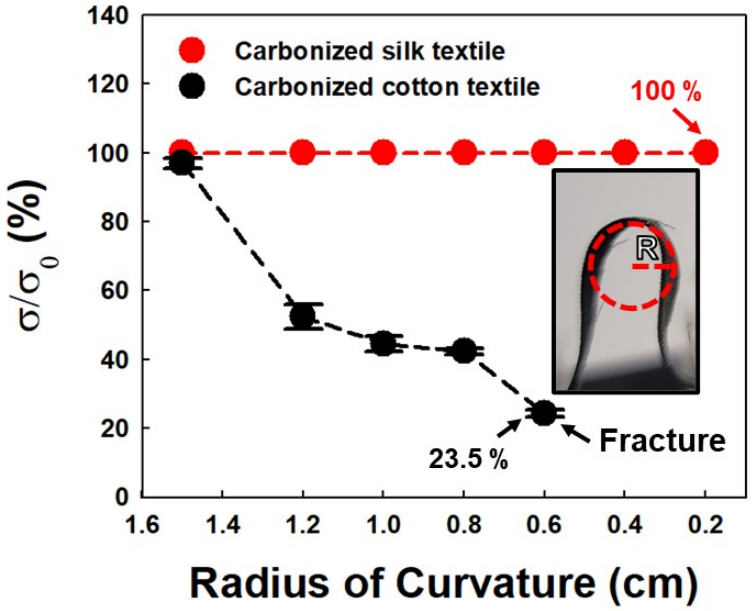

Fig. S3. Mechanical stability tests for CST and carbonized cotton textile. Relative electrical conductivity (σ/σ_0) of each carbonized textile as a function of the radius of curvature.

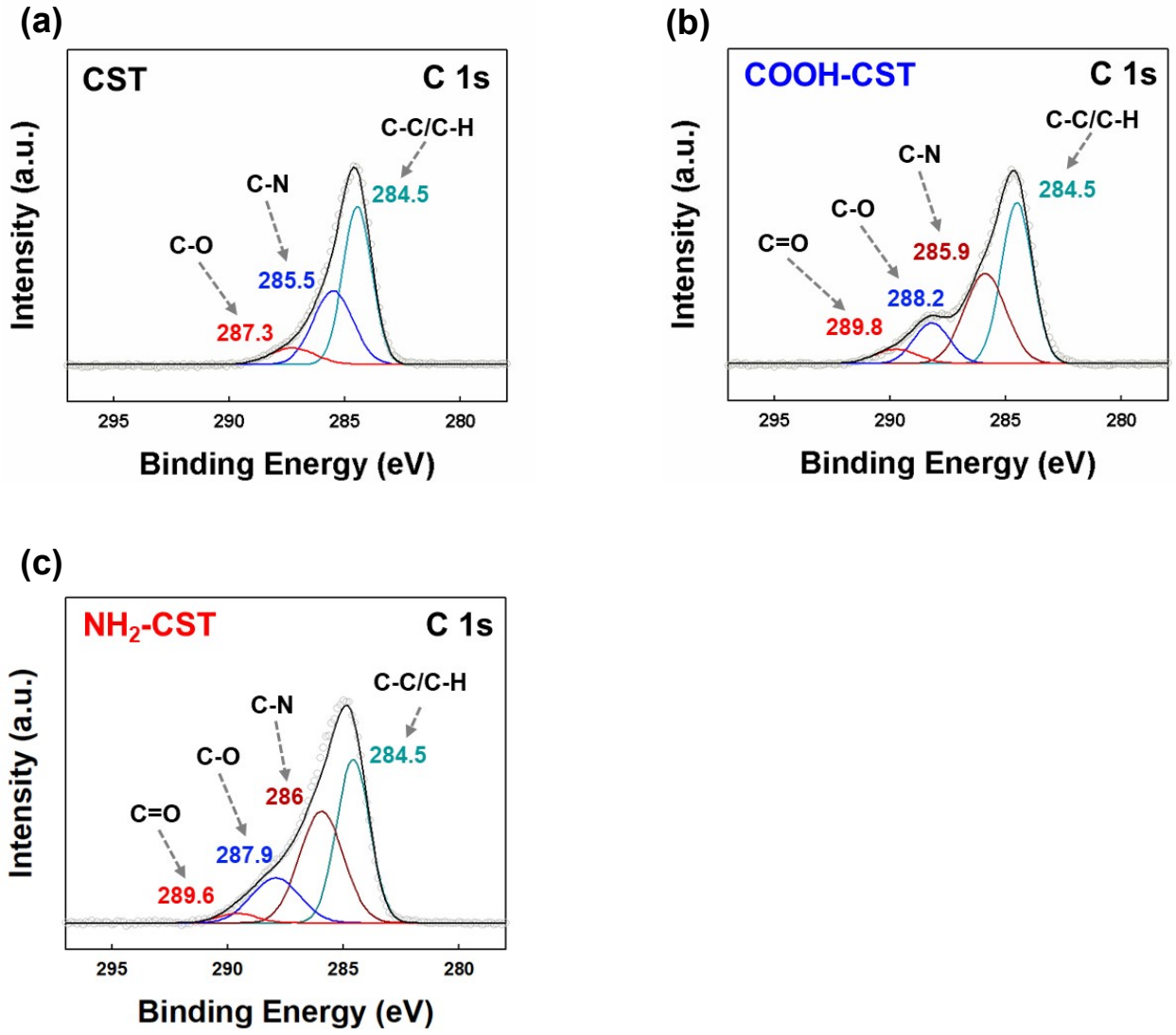

Fig. S4. XPS spectra of C 1s for (a) CST, (b) COOH–CST, and (c) NH_2–CST.

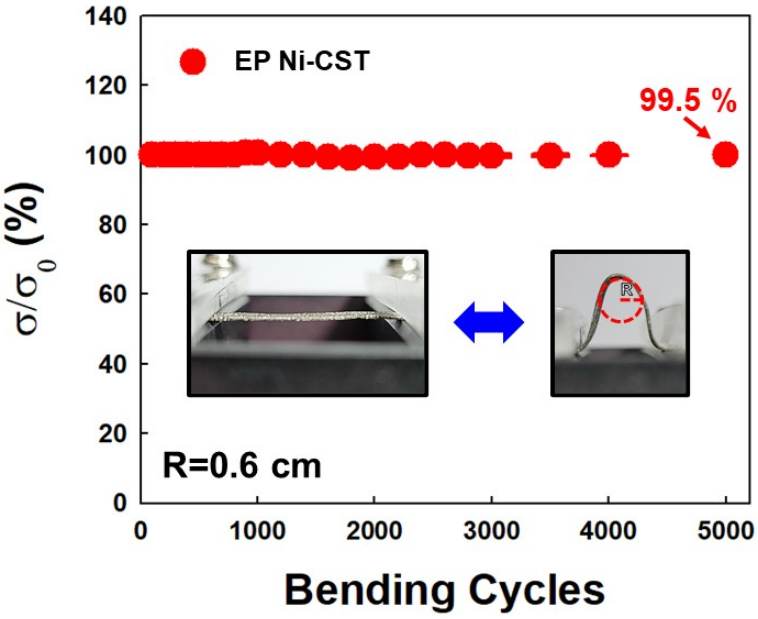

Fig. S5. Mechanical stability tests for the EP Ni–CST. Relative electrical conductivity (σ/σ_0) of EP Ni–CST electrode as a function of bending cycling number (bending radius of ~ 0.6 cm).

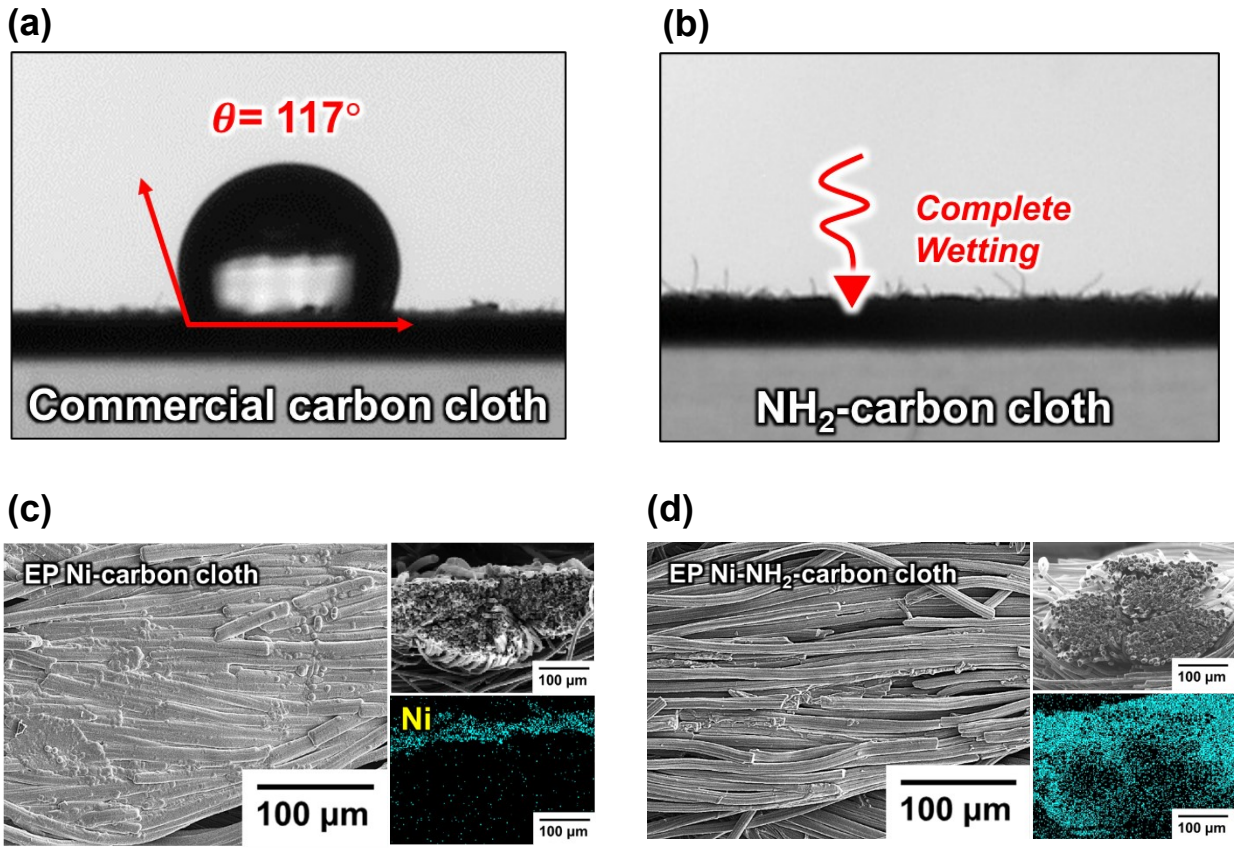

Fig. S6. (a) Water contact angles of commercial carbon cloth and (b) NH_2–carbon cloth. (c) FE-SEM images and energy-dispersive X-ray spectroscopy (EDX) mapping images of EP Ni–carbon cloth and (d) EP–NH_2–carbon cloth.

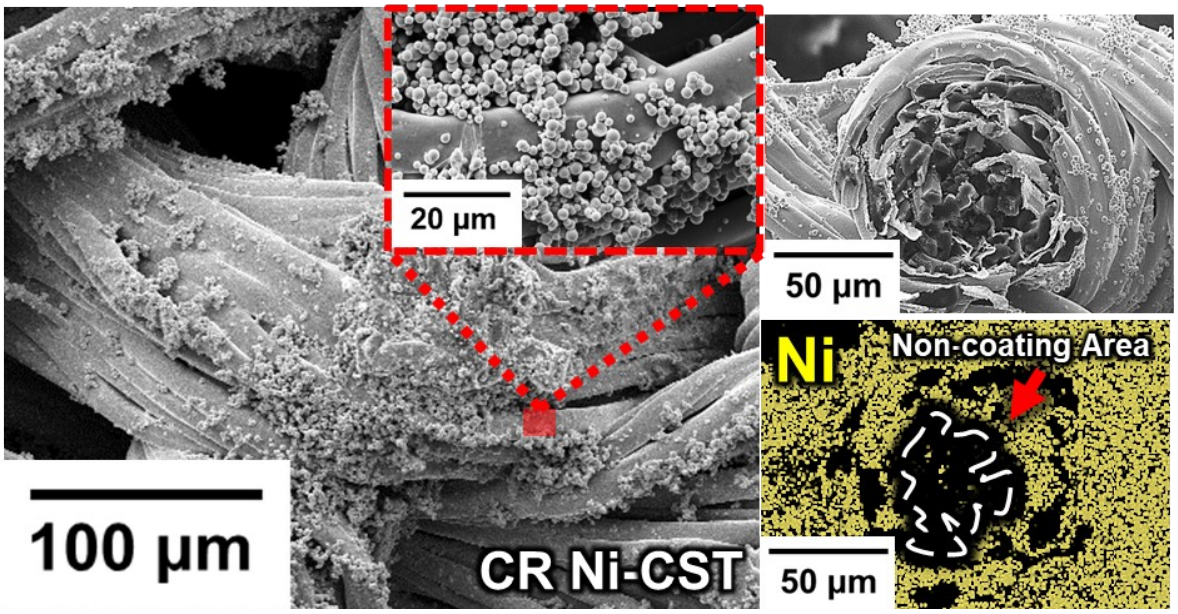

Fig. S7. FE-SEM images and energy-dispersive X-ray spectroscopy (EDX) mapping images of CR Ni–CST prepared from NH_2–CST.

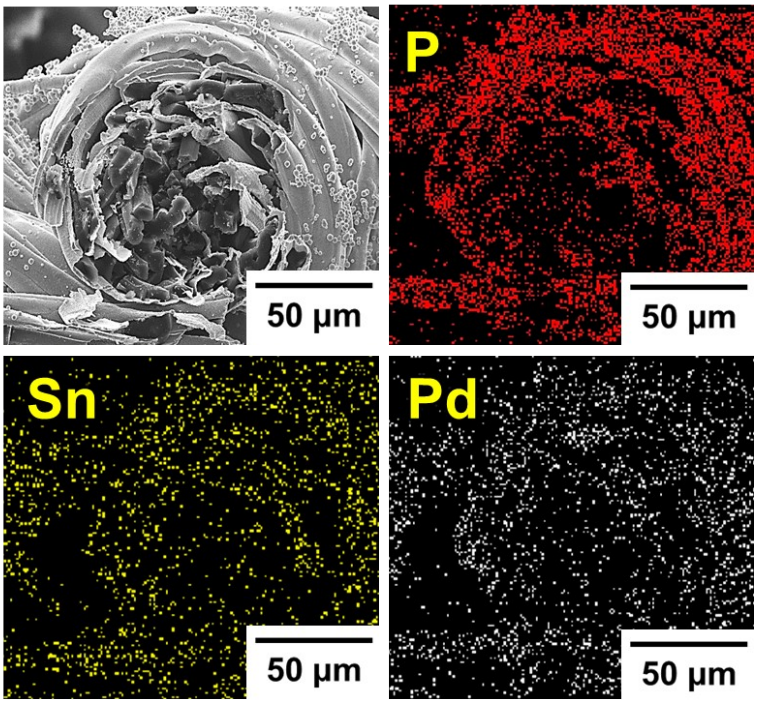

Fig. S8. Cross-sectional FE-SEM image and EDX mapping images of CR Ni–CST prepared from NH_2–CST.

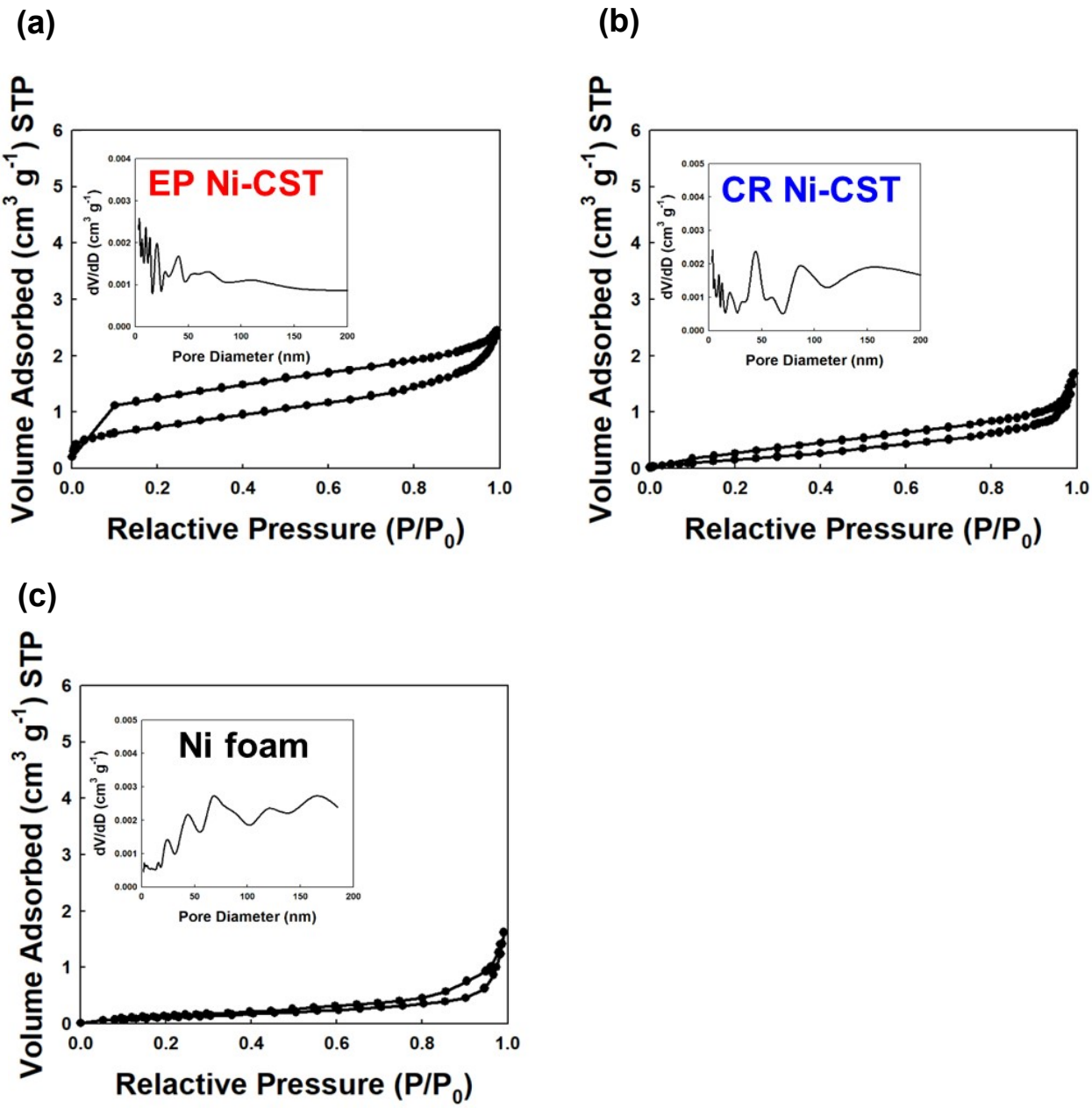

Fig. S9. BET data of EP Ni-CST, CR Ni-CST and commercial Ni foam. N_2 adsorption-desorption isotherms, and Barrett-Joyner-Halenda (BJH) pore size distributions of (a) EP Ni–CST, (b) CR Ni–CST and (c) commercial Ni foam. In this case, the pore size in the EP Ni–CST was distributed in the range from ~1 to ~ 200 nm with a distinct peak at 3.8, 10, 14.1, and 21.1 nm, which is smaller pore size than that of CR Ni–CST (i.e., 5, 44.7, 85.3, and 154.1 nm) and Ni foam (i.e., 43.6, 66.5, 119.5, and 163.2 nm). Moreover, the specific surface area of the EP Ni–CST was measured to be 4.45 $m^2\ g^{-1}$, which was approximately 5.6 times higher than that of the CR Ni–CST (0.8 $m^2\ g^{-1}$) and 9

times higher than that of Ni foam (0.5 m^2 g^{-1}). This increased specific surface of the EP Ni–CST was mainly attributed to the large amount of Ni protrusions created during the electroplating.

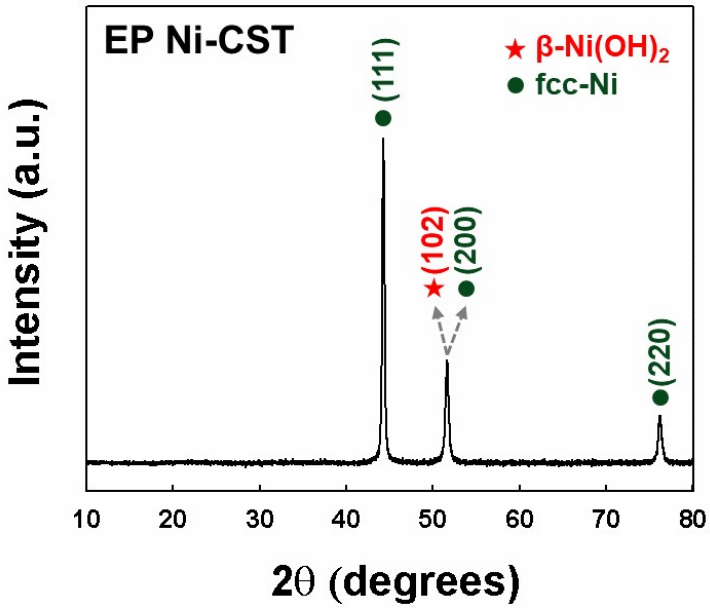

Fig. S10. XRD patterns of EP Ni–CST. In particular, at the 52°, the β-$Ni(OH)_2$ (102) peak was overlapped with face-centered cubic (fcc)-Ni (220).[S19.S20]

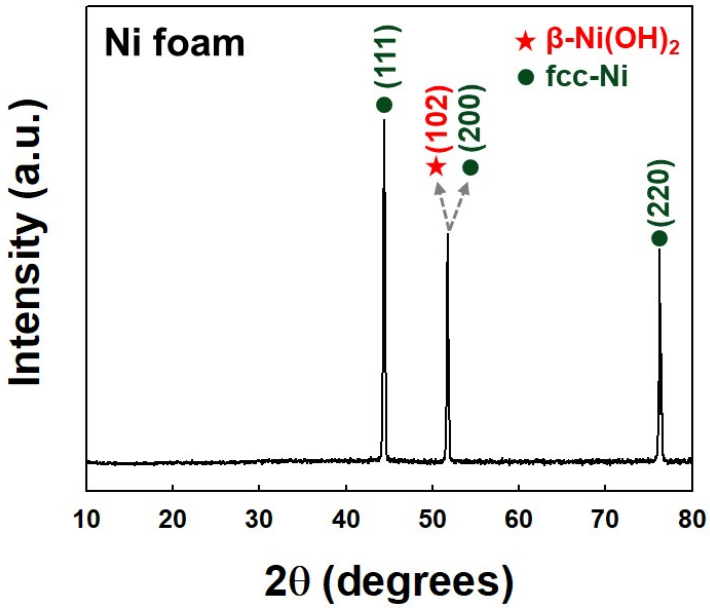

Fig. S11. XRD patterns for the Ni foam. In particular, at the 52°, the β-$Ni(OH)_2$ (102) peak was overlapped with fcc-Ni (220).[S19.S20]

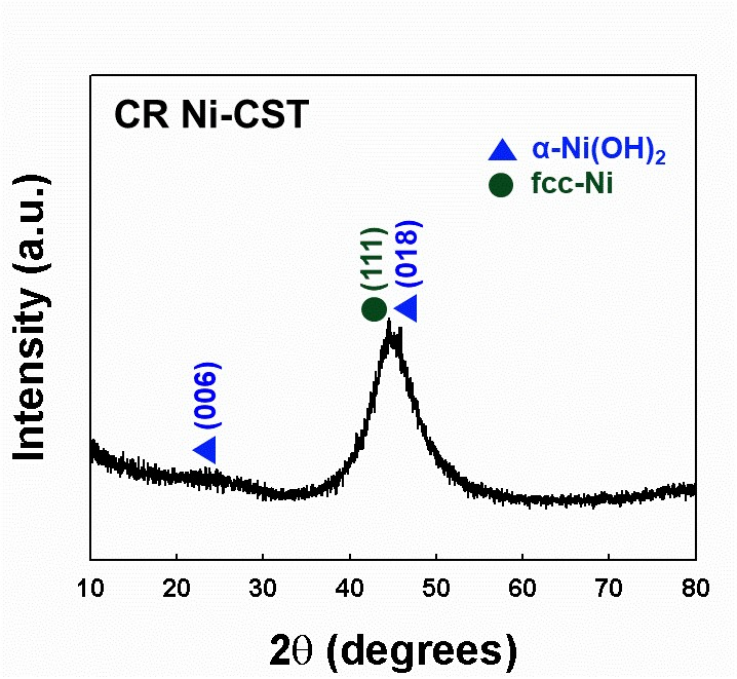

Fig. S12. XRD patterns for CR Ni–CST. In this case, the diffraction peaks at 22.5° and 46° match well with the (006) and (018) planes of α-$Ni(OH)_2$ (JCPDS 38-0715), respectively.

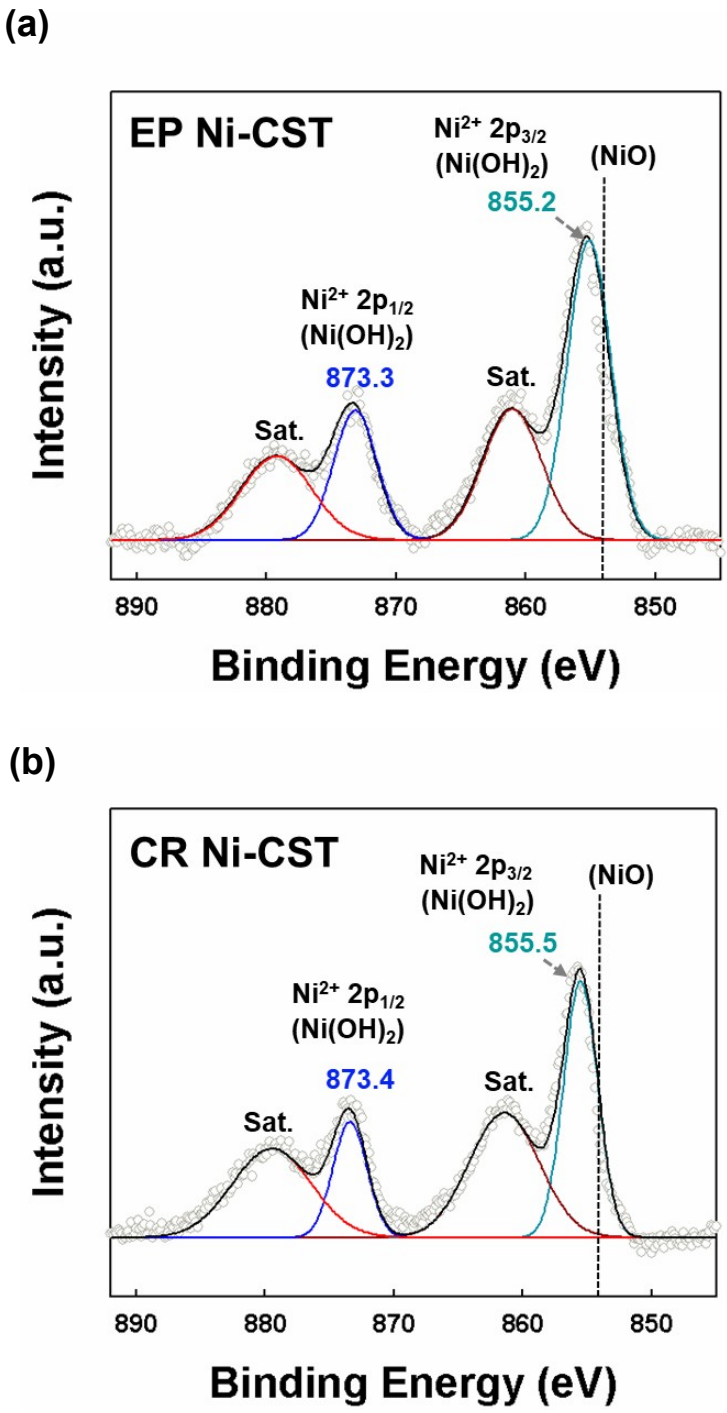

Fig. S13. XPS spectra of Ni 2p for the (a) EP Ni–CST and (b) CR Ni–CST.

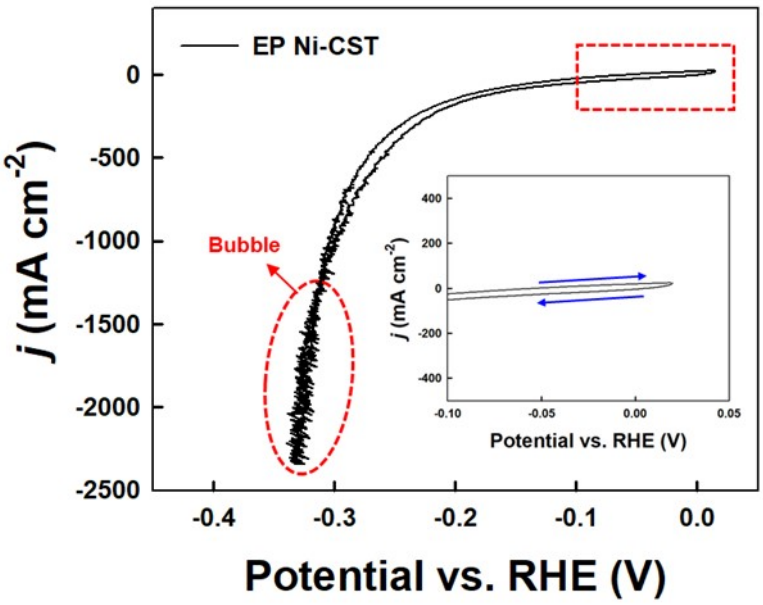

Fig. S14. Cyclic voltammetry curves of EP Ni–CST at a scan rate of 1 mV s^{-1} in 1 M KOH. In this case, the EP Ni–CST did not show any anodic or cathodic peaks except only negligible hysteresis in the given potential range, which implied the absence of parasitic reduction in the given potential range.

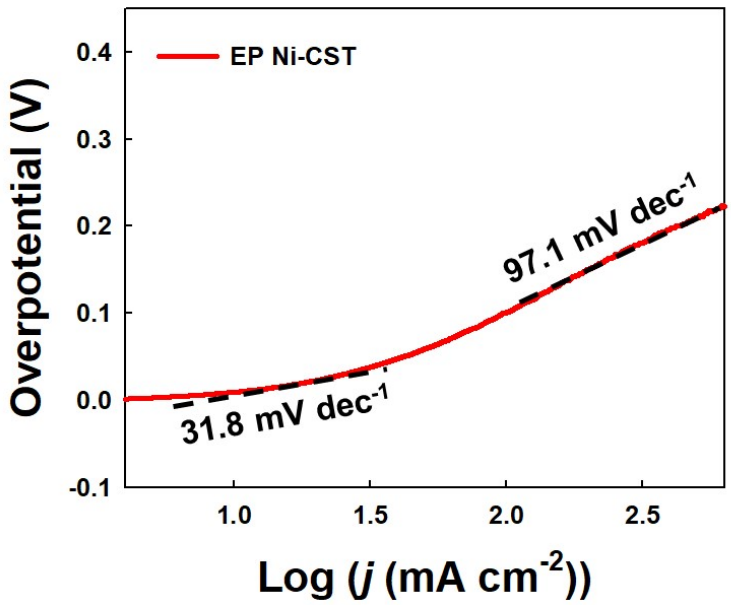

Fig. S15. Detailed Tafel slope analysis in a wide range of HER overpotentials. The EP Ni–CST exhibited Tafel slope of 31.8 mV dec^{-1} in the low overpotential range (< 35 mV), which implied that the Tafel step was the rate-limiting step. On the other hand, in high overpotential range (>150 mV), the EP Ni–CST showed Tafel slope of 97.1 mV dec^{-1}, indicating that the rate-limiting step is closely related to Volmer step. [S21,S22]

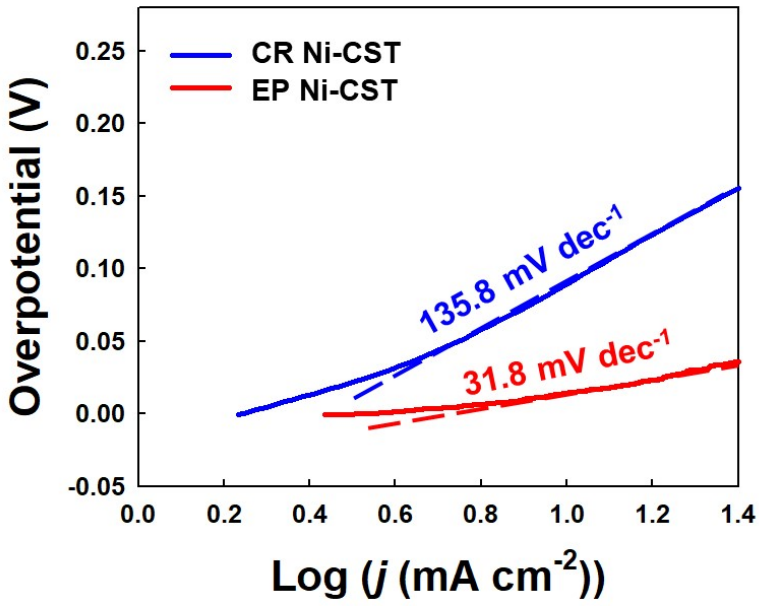

Fig. S16. Tafel plots for the CR Ni–CST and EP Ni–CST.

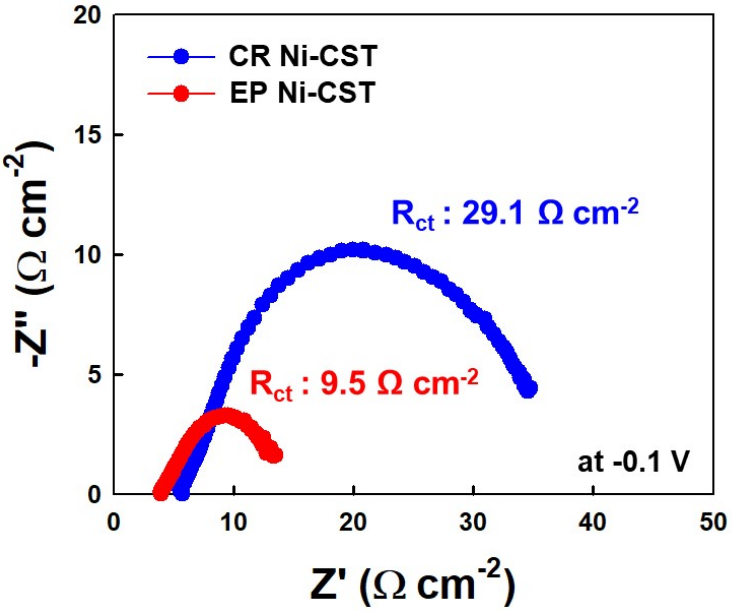

Fig. S17. EIS plots for the CR Ni–CST and EP Ni–CST at an applied potential of −0.1 V (vs. RHE).

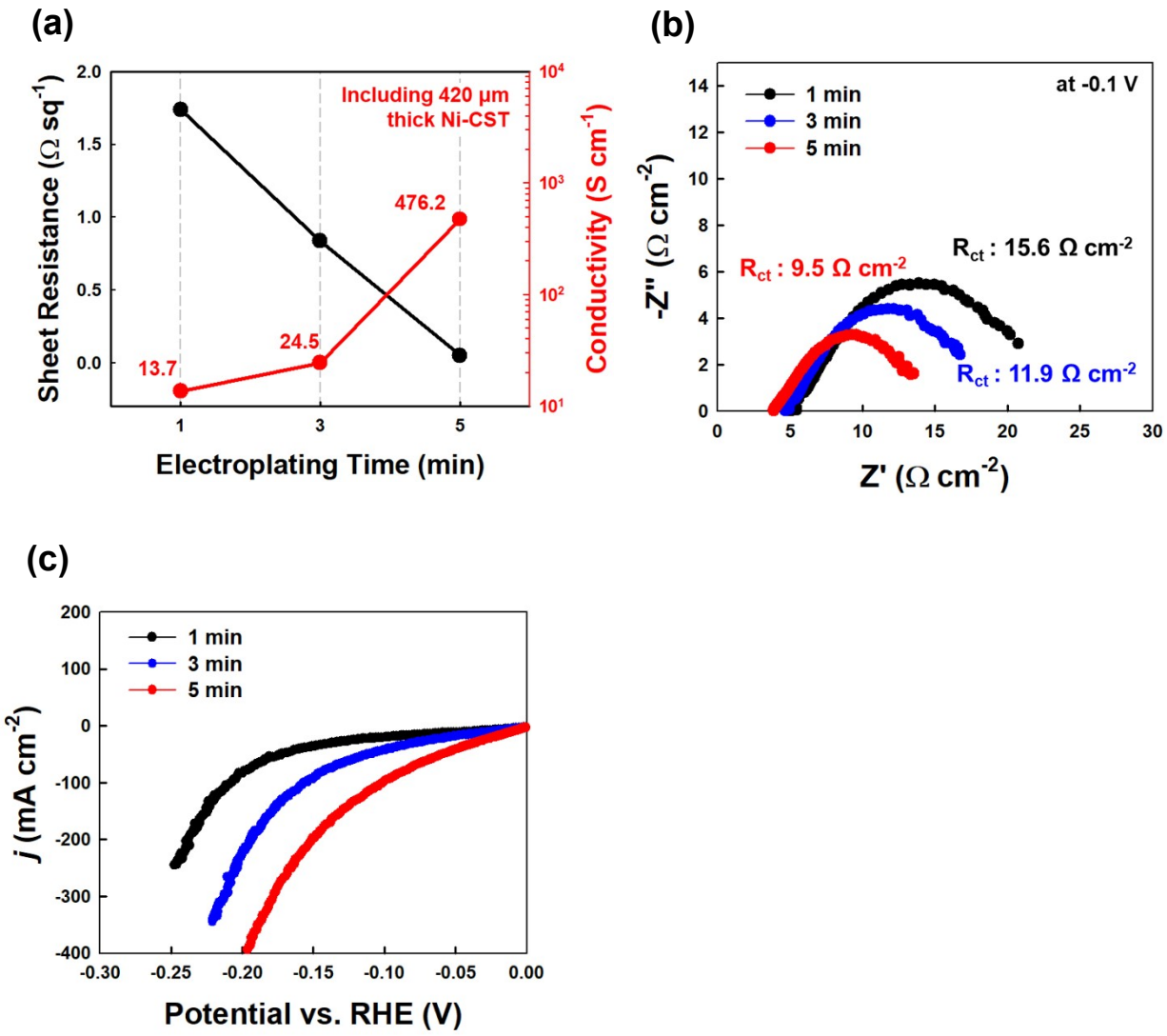

Fig. S18. (a) Sheet resistance and electrical conductivity of EP Ni–CST as a function of electroplating time at a current density of 360 mA cm^{-2}. (b) Electrochemical impedance spectroscopy (EIS) plots of the HER electrodes recorded at an applied potential of −0.1 V vs. RHE. (c) HER polarization curves of the EP Ni–CST electrodes in a 1 M KOH electrolyte. In this case, the electrical conductivity of Ni electroplated for 5 min onto the NH_2–CST (5 min-EP Ni–CST) was estimated to be approximately 476.2 S cm^{-1}, which was higher than those of 1 min-, and 3 min-EP Ni–CST. Furthermore, the 5 min-EP Ni–CST electrodes exhibited much lower charge transfer resistance (R_{ct}) of 9.5 Ω cm^{-2} than those of other electrodes. That is, the increased electrical conductivity of the EP Ni–CST was closely related to the enhancement of charge transfer efficiency during HER, which could lead to high electrocatalytic activity.

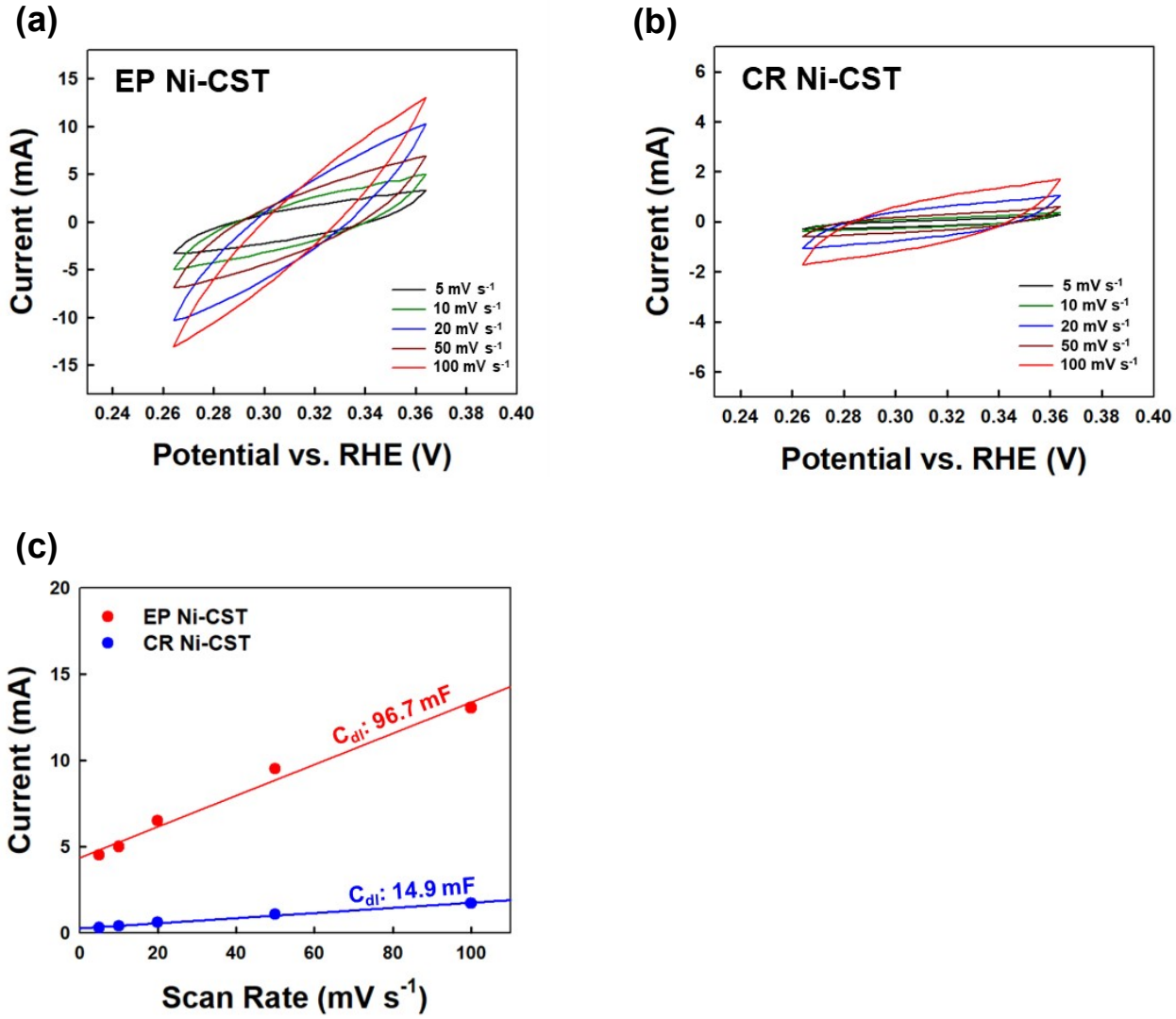

Fig. S19. Comparison of ECSA data of HER electrodes. CV curves recorded in the non-faradaic region (0.26–0.36 V) at different scan rates (5, 10, 20, 50 and 100 mV s^{-1}) for (a) EP and (b) CR Ni–CST. (c) Double-layer capacitance (C_{dl}) for the electrodes measured at different scan rates. Based on the specific capacitance of 0.040 mF cm^{-2} of Ni, the ECSA of EP Ni–CST and CR Ni–CST were calculated to be approximately 2417.5 cm^2 and 372.5 cm^2, respectively.

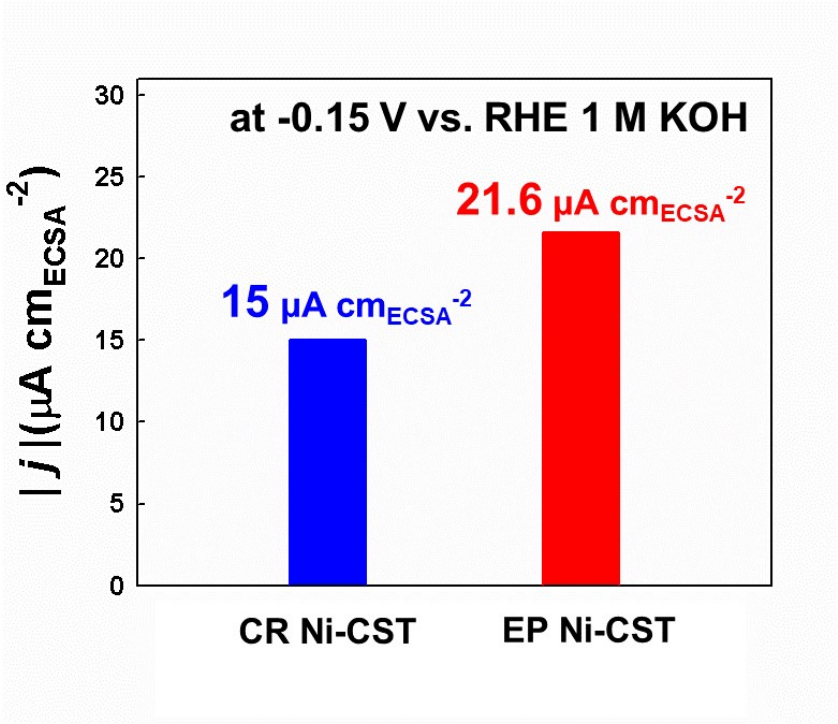

Fig. S20. Intrinsic HER activity (μA cm^{-2}_{ECSA}) of CR Ni–CST and EP Ni–CST normalized with respect to the ECSAs of the electrocatalysts. In this case, |*j*| is defined as absolute value of the current density normalized with respect to the ECSAs

(a)

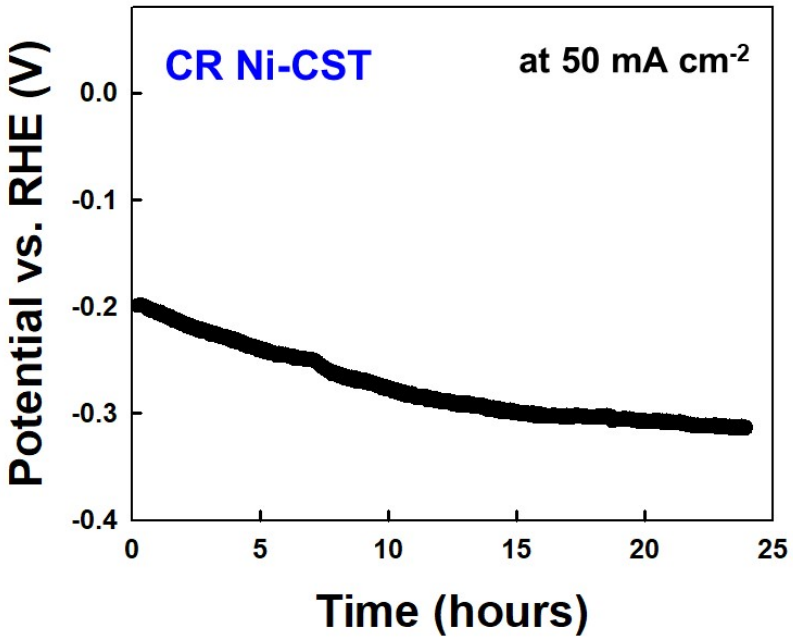

(b)

	EP Ni–CST	CR Ni–CST
Ni	Not detected	17.7 μg L^{-1}

Fig. S21. (a) Chronopotentiometry curves of CR Ni–CST at 50 mA cm^{-2}. (b) ICP-MS data of electrolyte (KOH) after hydrogen evolution reaction (HER).

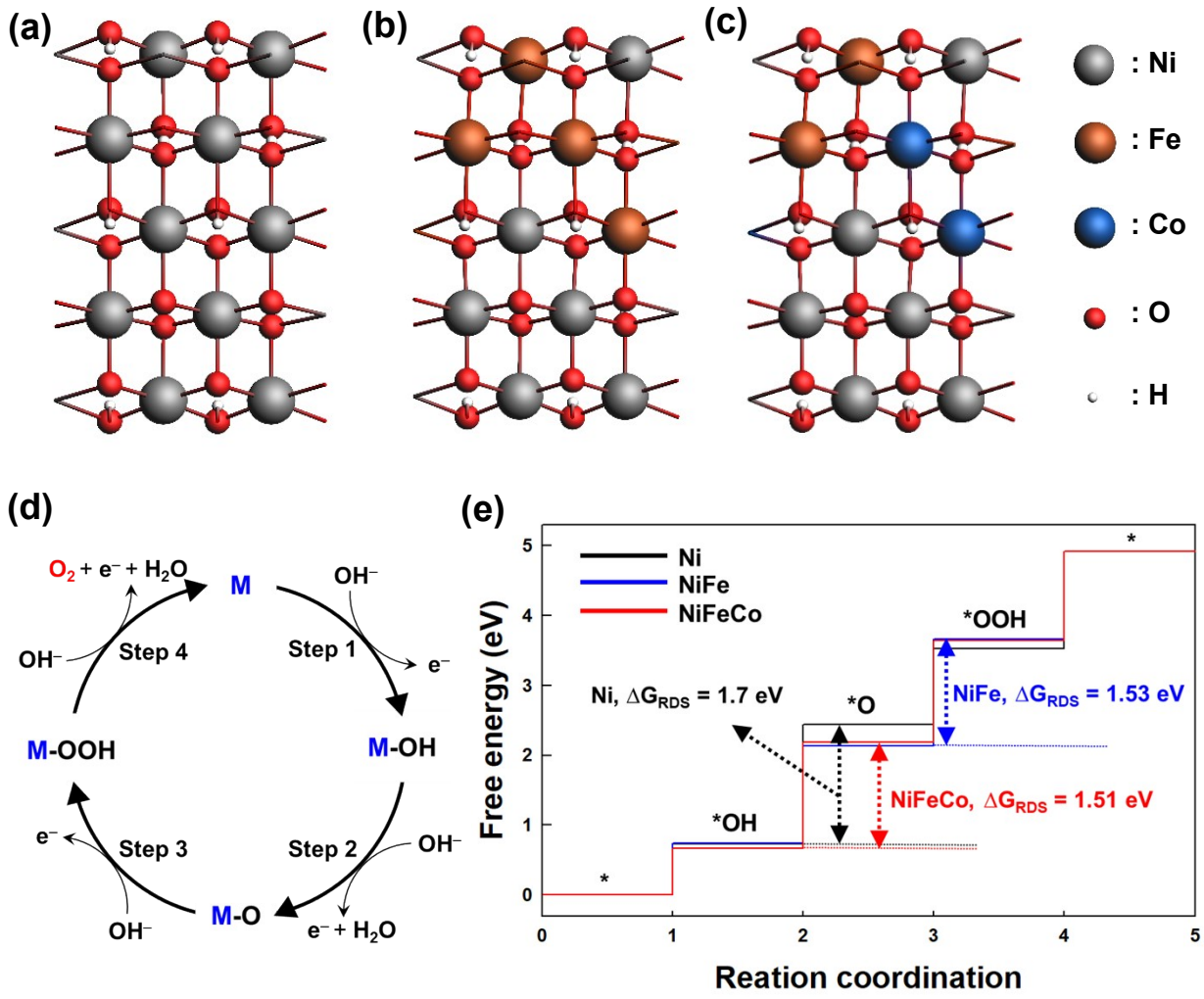

Fig. S22. The structures of (a) Ni, (b) NiFe, and (c) NiFeCo. (d) 4-step OER mechanism in alkaline media.[S23] Herein, M means the active site. (e) Calculated Gibbs free-energy diagram of OER on Ni (black line), NiFe (blue line), and NiFeCo (red line).[S16] Considering that the rate determining step is determined by the largest Gibbs free energy difference, the rate determining step of Ni, NiFe, and NiFeCo correspond to step 2, 3, and 2, respectively. Particularly, the Gibbs free energy difference values of Ni (1.7 eV) and NiFe (1.53 eV) are larger than that of the NiFeCo (1.51 eV), which demonstrate that the NiFeCo needs a lower overpotential to drive the OER. As a results, the NiFeCo can operate as more active catalytic sites, boost OER catalytic activity, and optimize the adsorption of *OH and *O intermediates.

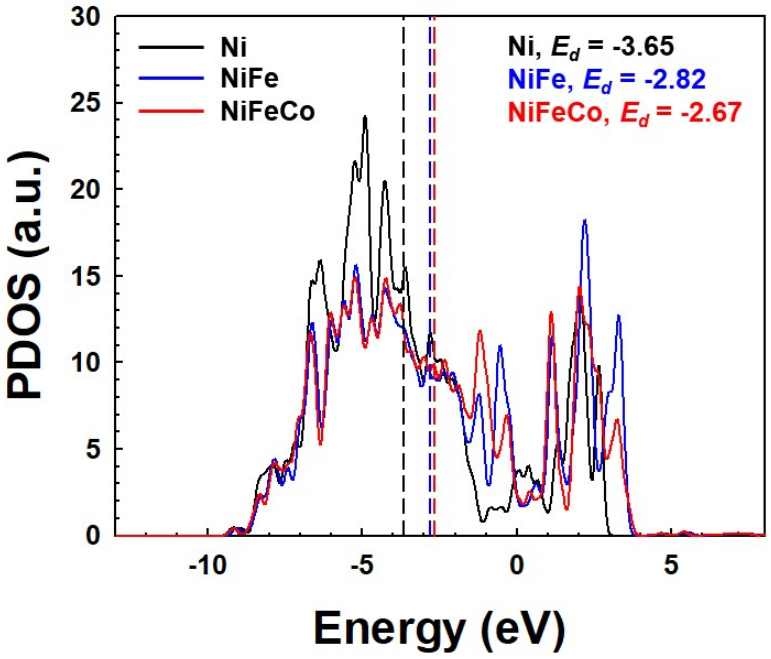

Fig. S23. Projected density of states (PDOS) curves of *d*-orbital for Ni, NiFe and, NiFeCo-based catalyst. Dashed lines colored black, blue, and red represent *d*-band center (E_d) for Ni, NiFe and, NiFeCo-based catalyst, respectively. The bandgap between valence and conduction bands of NiFeCo was calculated to be approximately 0.188 eV, and on the other hand the bandgaps of NiFe and Ni were approximately 0.233 eV and 1.360 eV, respectively. These results show that the electrical conductivity of NiFeCo catalyst is higher than those of Ni and NiFe catalysts. Furthermore, the E_d of the NiFeCo is shifted to the higher energy (-2.67 eV) compared to those of NiFe (-2.82 eV) and Ni (-3.65 eV), which means that the NiFeCo has a narrower energy gap between *d*-band center (E_d) and Fermi level (E_F) than NiFe and Ni. These results evidently show that the NiFeCo can further effectively regulate the electronic structure through the additional doping of Fe and/or Co within Ni, which can optimize the adsorption properties of intermediate reactants during electrocatalytic process.

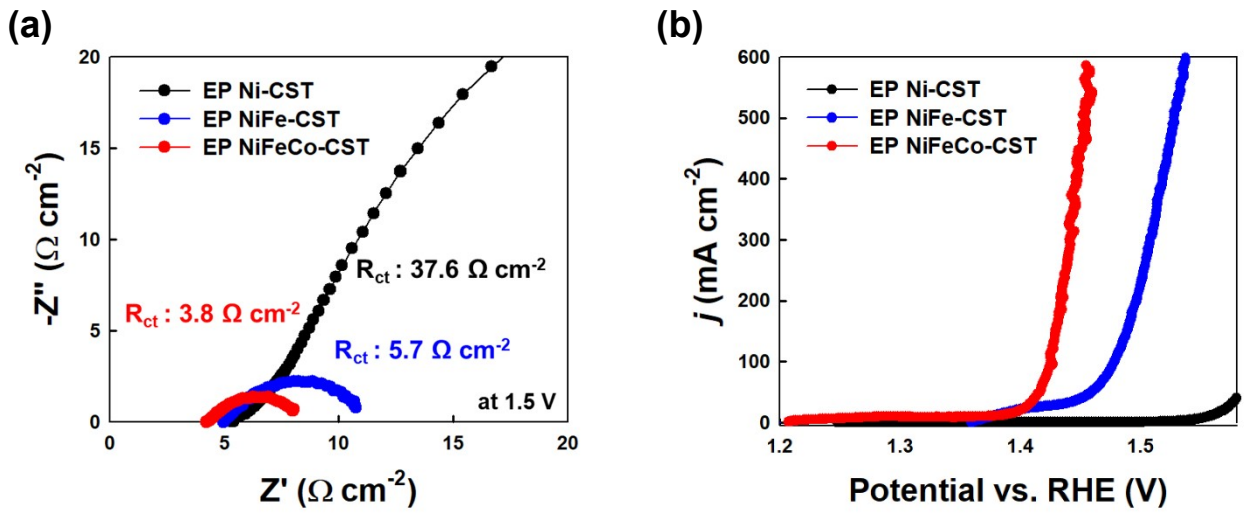

Fig. S24. (a) EIS plots of the OER electrodes recorded at an applied potential of 1.5 V vs. RHE. (b) OER polarization curves of the EP Ni–CST, EP NiFe–CST and EP NiFeCo–CST electrodes in a 1 M KOH electrolyte. Based on PDOS data (**Fig. S23**), we additionally confirmed that the R_{ct} of the EP NiFeCo–CST was measured to be approximately 3.8 Ω cm^{-2}, which is extremely lower than those of the EP NiFe–CST (R_{ct} = 5.7 Ω cm^{-2}) and EP Ni–CST (R_{ct} = 37.6 Ω cm^{-2}). It could be attributed to that proper Fe and Co doping into Ni could not only enhance the electrical conductivity but also make the more favorable charge transfer process during OER, which induce high electrocatalytic activity.

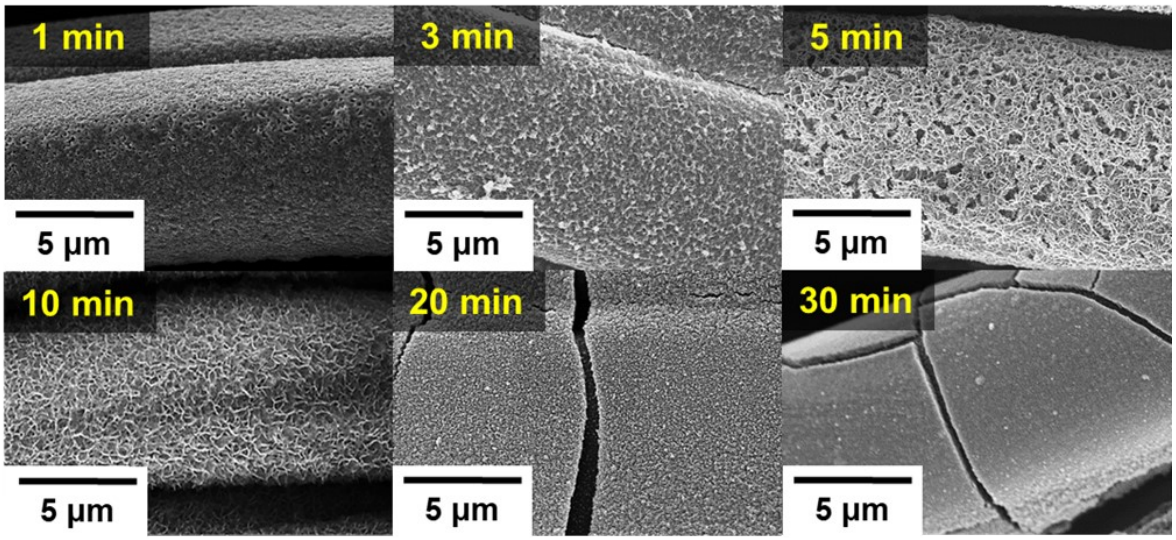

Fig. S25. Planar FE-SEM images of EP NiFeCo–CST as a function of electroplating time at 30 mA cm^{-2}.

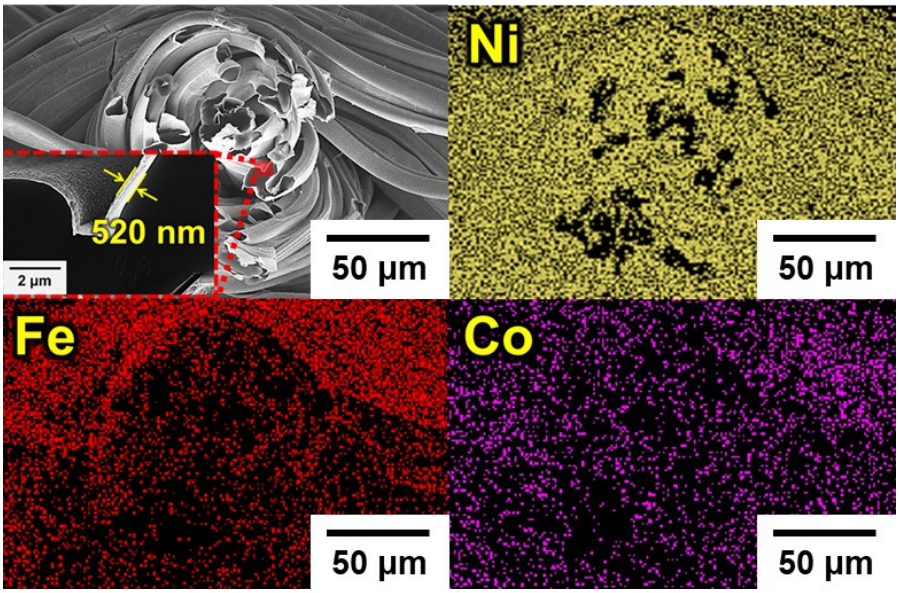

Fig. S26. Cross-sectional FE-SEM images and EDX mappings of EP NiFeCo–CST (the inset shows the thickness of the NiFeCo/Ni layer).

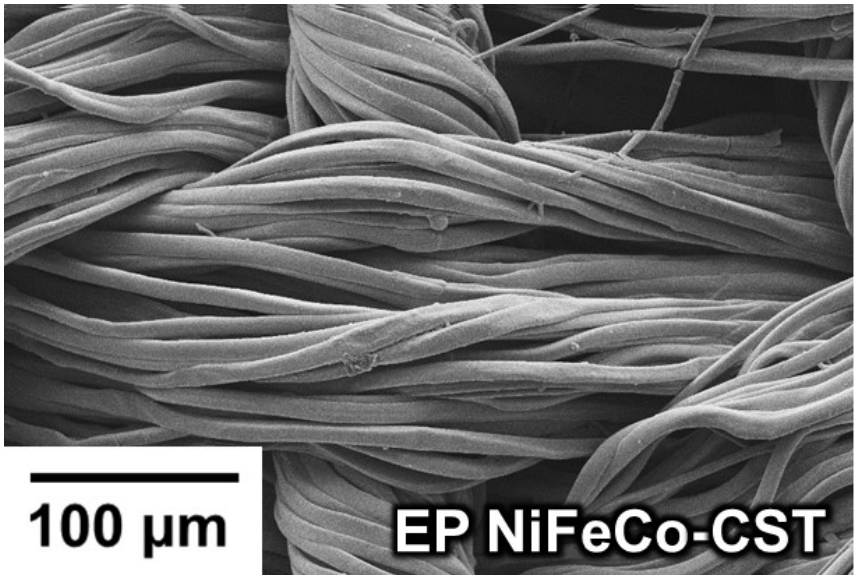

Fig. S27. Planar FE-SEM image of EP NiFeCo–CST.

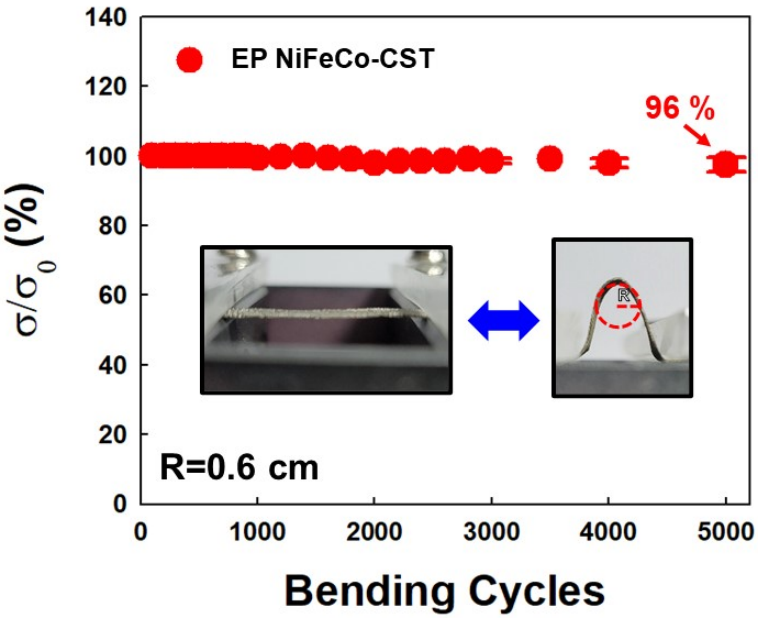

Fig. S28. Mechanical stability tests for the EP NiFeCo–CST. Relative electrical conductivity (σ/σ_0) of the electrode as a function of bending cycling number (bending radius of ~ 0.6 cm).

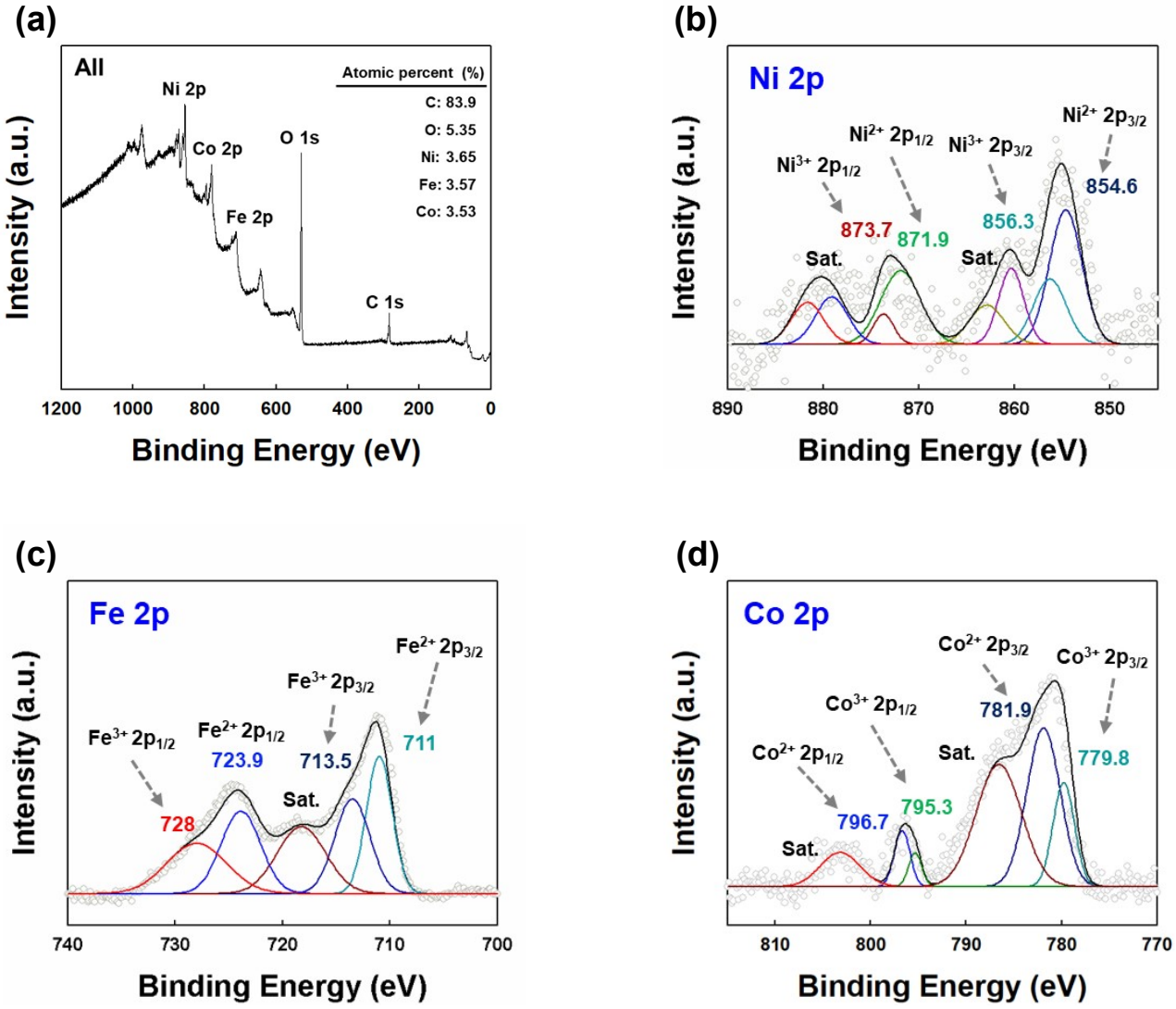

Fig. S29. (a) XPS survey spectra of EP NiFeCo–CST. High-resolution XPS spectra of (b) Ni 2p, (c) Fe 2p and (d) Co 2p for the EP NiFeCo–CST.[S24-S26]

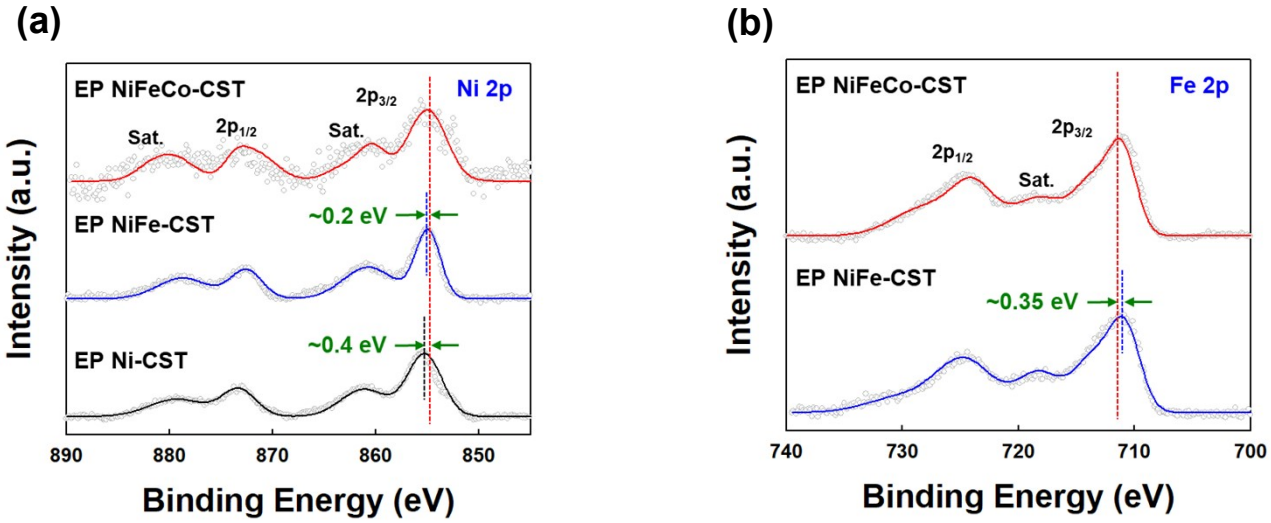

Fig. S30. XPS spectra of (a) Ni 2p of EP Ni–, EP NiFe–, and EP NiFeCo–CST electrodes and (b) Fe 2p of EP NiFe–, and EP NiFeCo–CST electrodes. In general, the shift of XPS peak in the doped sample reflects a change in electronic configuration and electron transfer between cations, indicating the existence of electronic interaction between neighboring elements after doping.[S27] As shown in **Fig. S30a**, the Ni $2p_{3/2}$ peak of EP NiFeCo–CST was shifted to the lower binding energy (~0.4 eV) compared to those of EP Ni–, EP NiFe–CST. The larger electronegativity of metal element can induce the formation of the more active metal element, which resultantly can more strongly attract electrons. These phenomena were consistent with the previous results that the XPS peak for Ni in EP NiFeCo–CST was shifted to the lower binding energy.[S27]

On the other hand, the Fe 2p spectrum of EP NiFeCo–CST exhibits the two distinct peaks Fe $2p_{1/2}$ and Fe $2p_{3/2}$, indicating that the Fe 2p peaks were shifted to the higher binding energies (~0.35 eV) compared to EP NiFe–CST (**Fig. S30b**). These peak shifts were mainly due to the charge redistribution at the Ni and Fe atomic sites, implying that the strong electronic interactions among Ni, Fe, and Co lead to the optimal adsorption energy of reaction intermediates for improving catalyst performance.[S28]

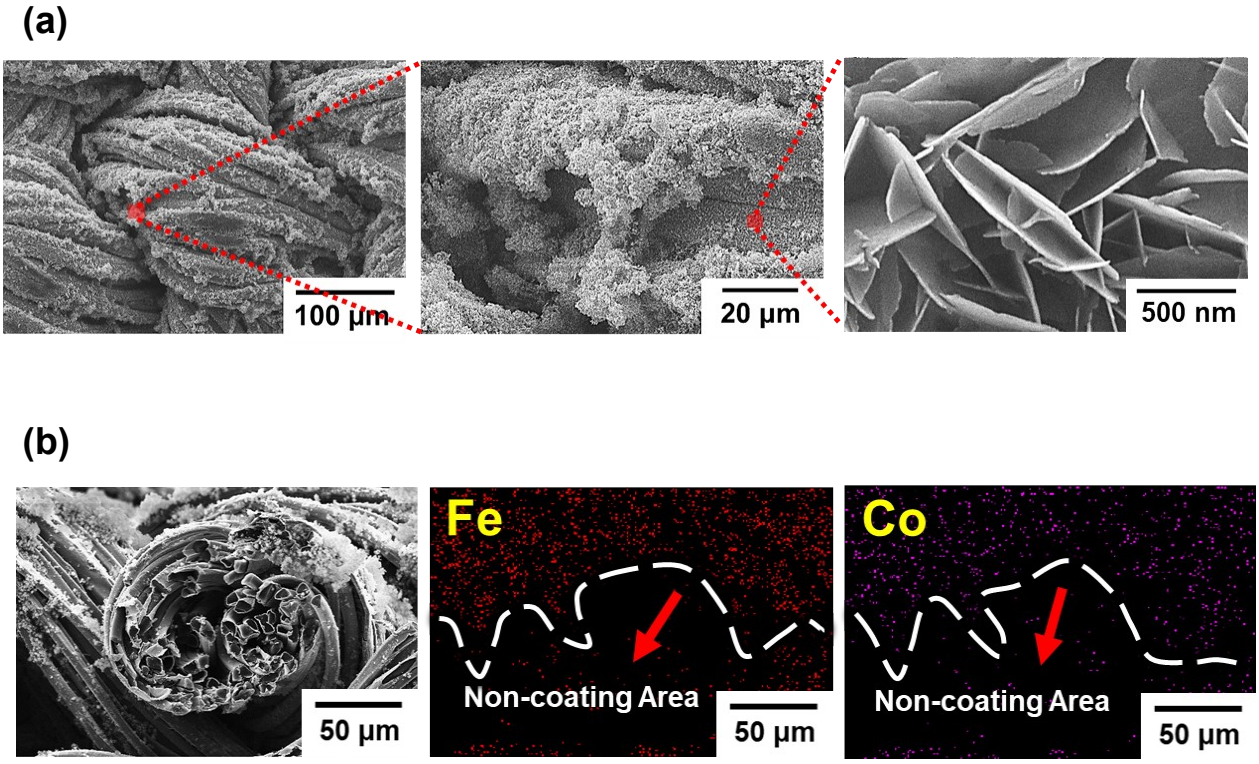

Fig. S31. (a) Planar FE-SEM images for the hydrothermal NiFeCo–CST. (b) Cross sectional FE-SEM image and corresponding EDX maps for the hydrothermal NiFeCo–CST.

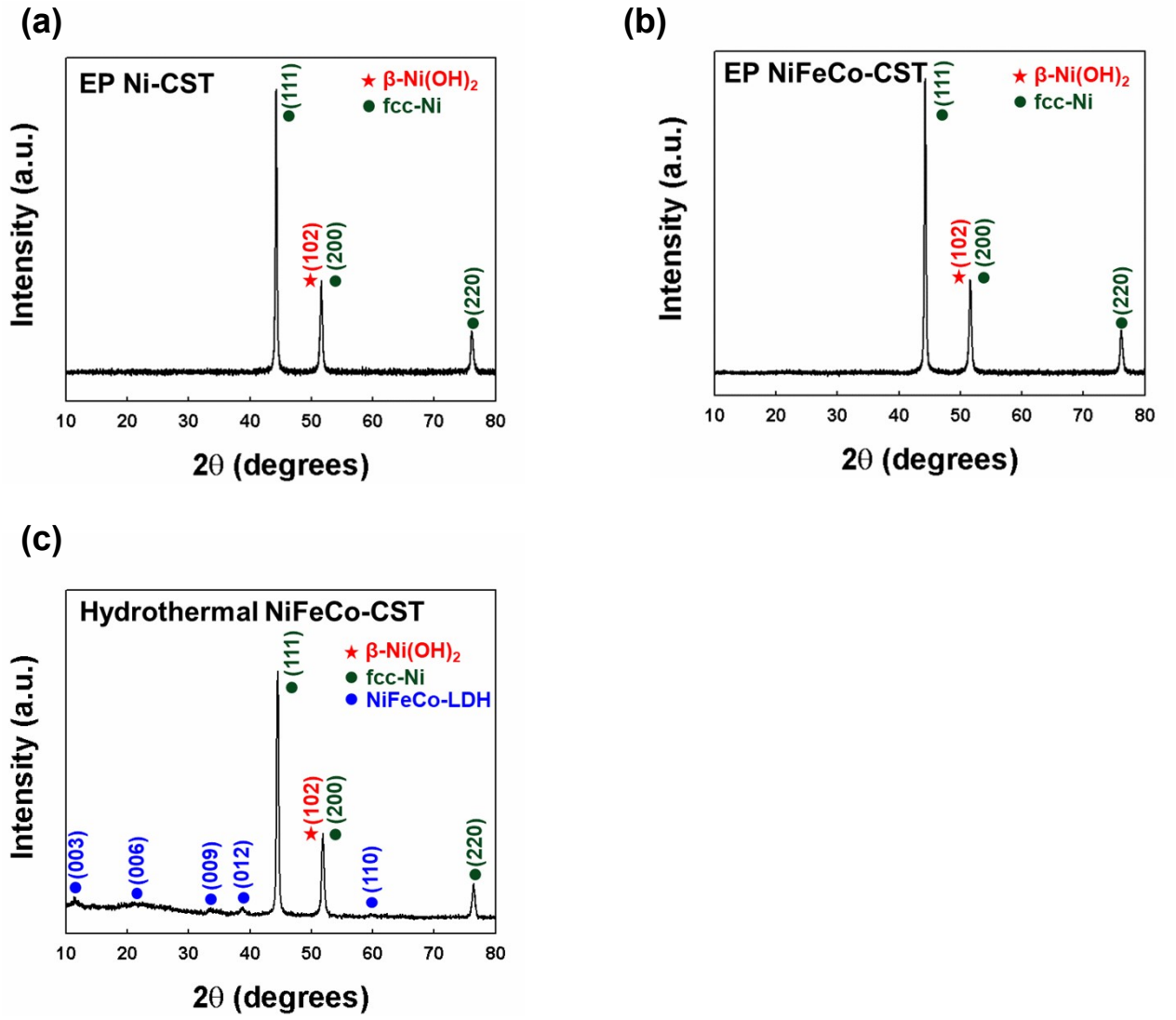

Fig. S32. XRD spectra of (a) EP Ni–CST, (b) EP NiFeCo–CST, and (c) Hydrothermal NiFeCo–CST.[S29]

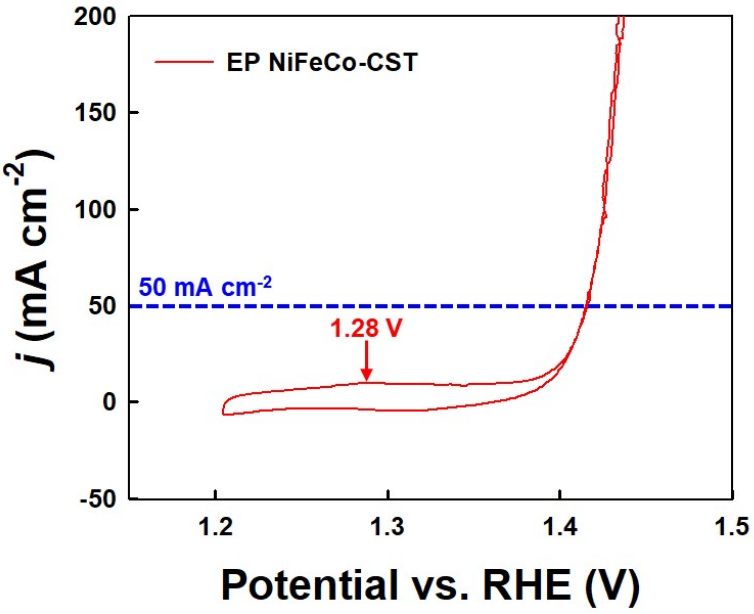

Fig. S33. OER CV curve of EP NiFeCo–CST in 1 M KOH. The anodic sweep exhibits a broad oxidation peak at approximately 1.28 V vs RHE. In general, the pure $Ni(OH)_2$ has an oxidation peak at 1.3–1.4 V vs RHE, which are attributed to the transformation between $Ni(OH)_2$ and NiOOH ($Ni(OH)_2 + OH^- \leftrightarrow NiOOH + H_2O + e^-$) in alkaline electrolytes.[S30] Furthermore, the pure $Co(OH)_2$ has two oxidation peaks at 1.22 V and 1.41 V vs RHE, which are attributed to i) the transformation between $Co(OH)_2$ and CoOOH ($Co(OH)_2 + OH^- \leftrightarrow CoOOH + H_2O + e^-$), and ii) the Co^{3+}/Co^{4+} redox couple in alkaline electrolyte.[S31,S32] However, in the case of the EP NiFeCo–CST, it has only one broad oxidation peak as mentioned above. This reason can be explained as follows.

As Fe is incorporated into the Co matrix, the position of the redox peak ($Co(OH)_2 \leftrightarrow$ CoOOH) is changed from 1.22 V (i.e., pure $Co(OH)_2$) to 1.28 V with increasing the content of Fe. Furthermore, it has been reported that the second oxidation peak (at 1.41 V) originating from the Co^{3+}/Co^{4+} redox couple significantly decreases with increasing the Fe content.[S33] Particularly, F. Dionigi *et al.* have reported that the CoFe LDH has a main oxidation peak at 1.35 V vs RHE and the corresponding peak occurs clearly prior to the onset of OER.[S32] Thus, the EP NiFeCo–CST has a broad oxidation peak by Co and Fe. To minimize the effect of the redox peak, the OER performance was investigated at a higher current density ($\geq$ 50 mA cm^{-2}) than 10 mA cm^{-2}.

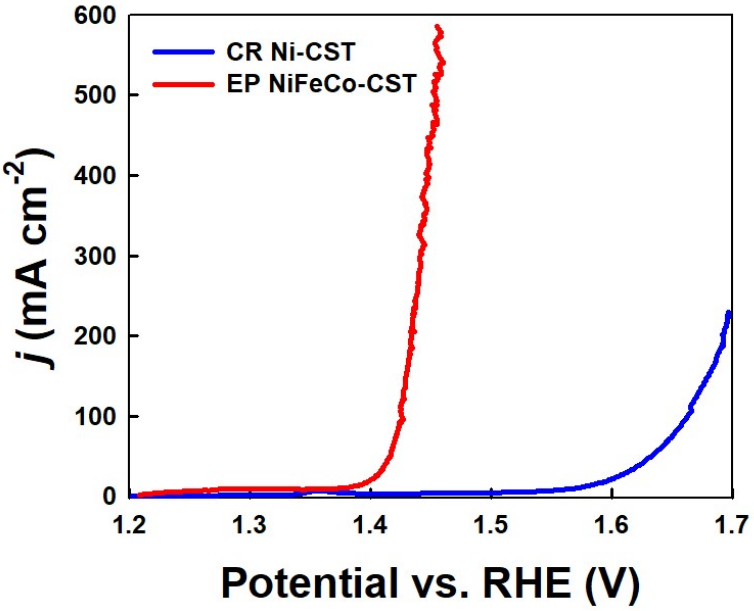

Fig. S34. OER polarization curves recorded with EP NiFeCo–CST and CR Ni–CST electrodes in a 1 M KOH electrolyte at a scan rate of 2 mV s^{-1}.

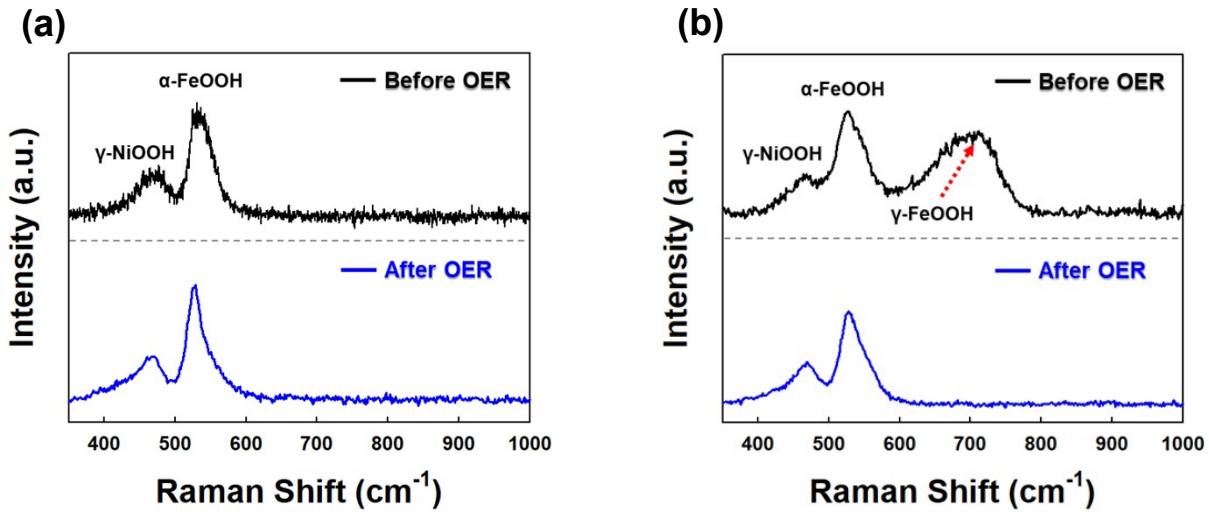

(c)

	EP NiFeCo–CST	**Hydrothermal NiFeCo–CST**
Fe	Not detected	158 μg L^{-1}
Ni	Not detected	2.88 μg L^{-1}
Co	Not detected	14.5 μg L^{-1}

Fig. S35. (a) Raman spectra of EP NiFeCo–CST and (b) Hydrothermal NiFeCo–CST. (c) ICP-MS data of electrolyte (KOH) after oxygen evolution reaction (OER).

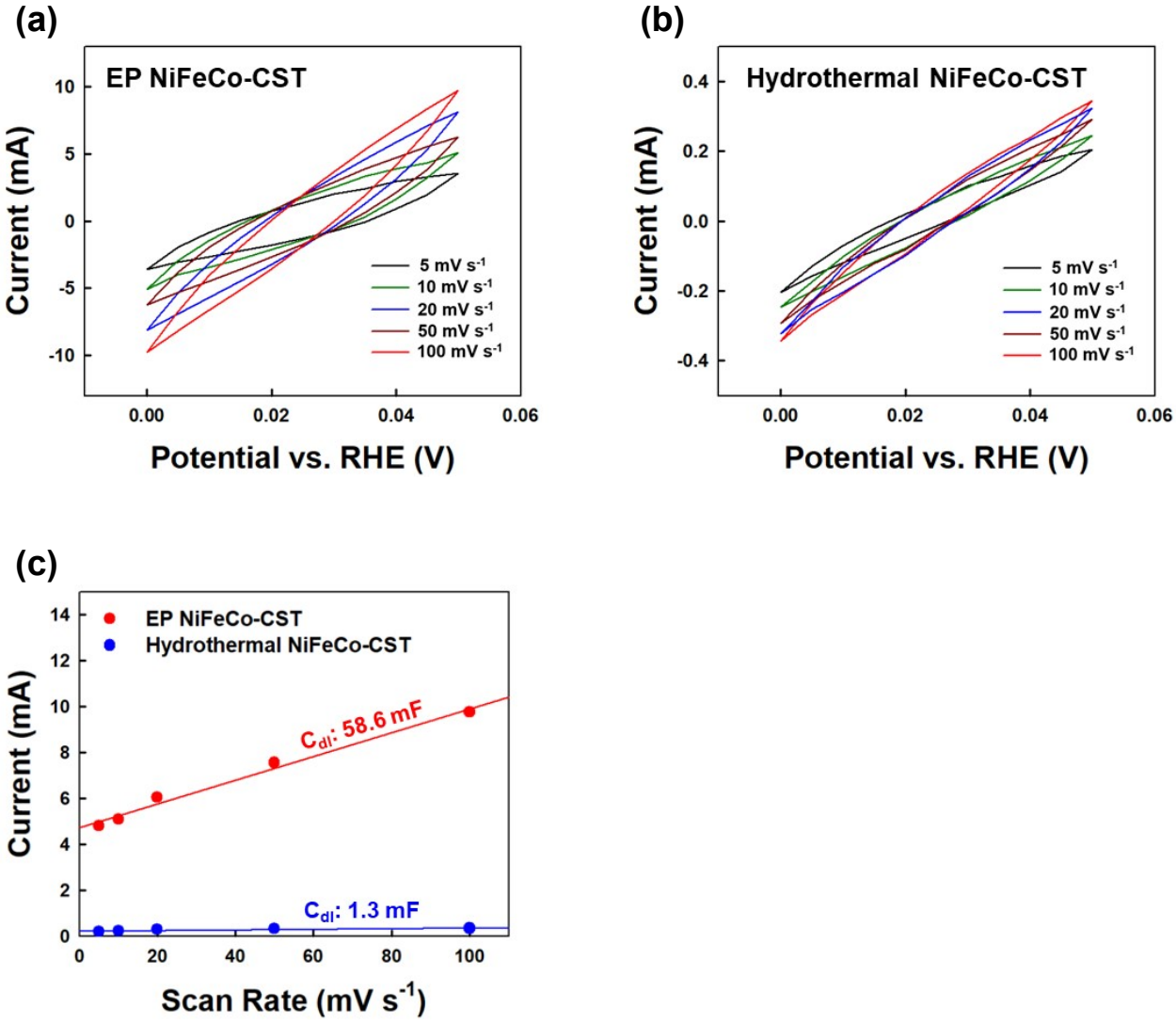

Fig. S36. Comparison of ECSA data of the electrodes. CV curves recorded in the non-faradaic region (0–0.05 V) at different scan rates (5, 10, 20, 50 and 100 mV s^{-1}) for (a) EP NiFeCo–CST and (b) hydrothermal NiFeCo–CST. (c) Double-layer capacitance (C_{dl}) for the electrodes measured at different scan rates.

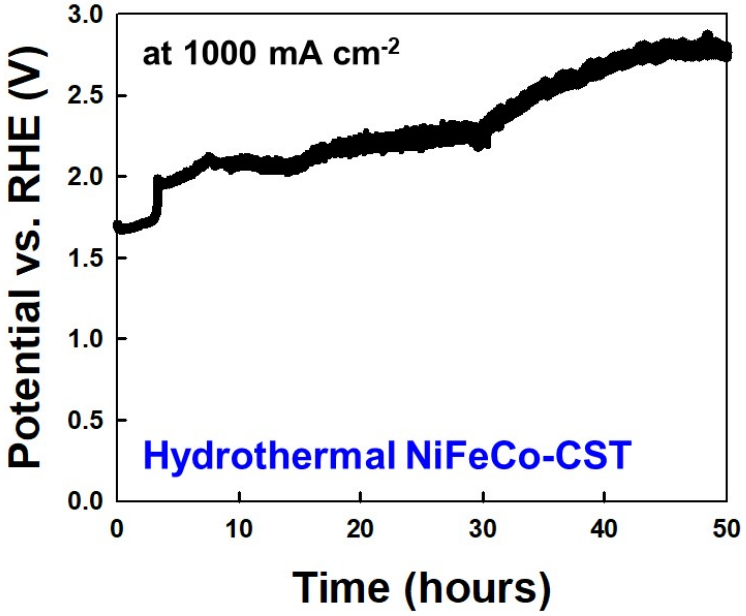

Fig. S37. Chronopotentiometry curve of hydrothermal NiFeCo–CST at 1000 mA cm^{-2}.

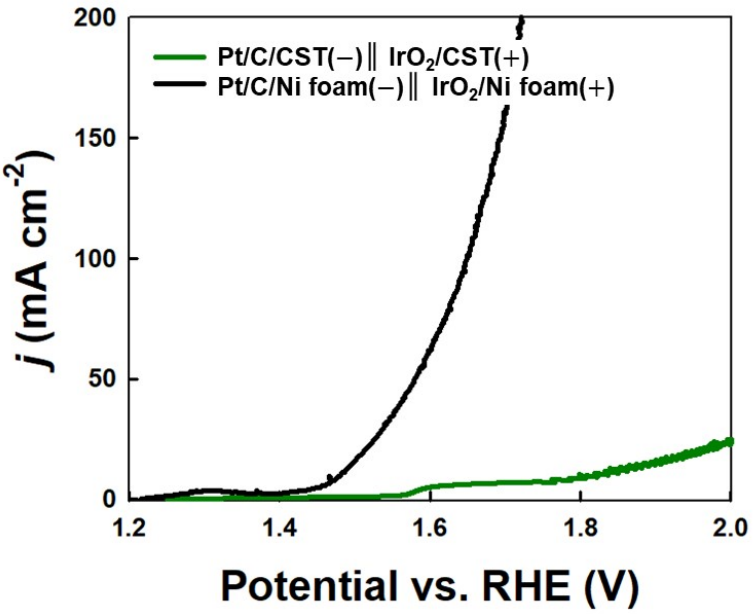

Fig. S38. Polarization curves of the Pt/C/CST‖IrO_2/CST and Pt/C/Ni foam‖IrO_2/Ni foam electrodes for water-splitting performance.

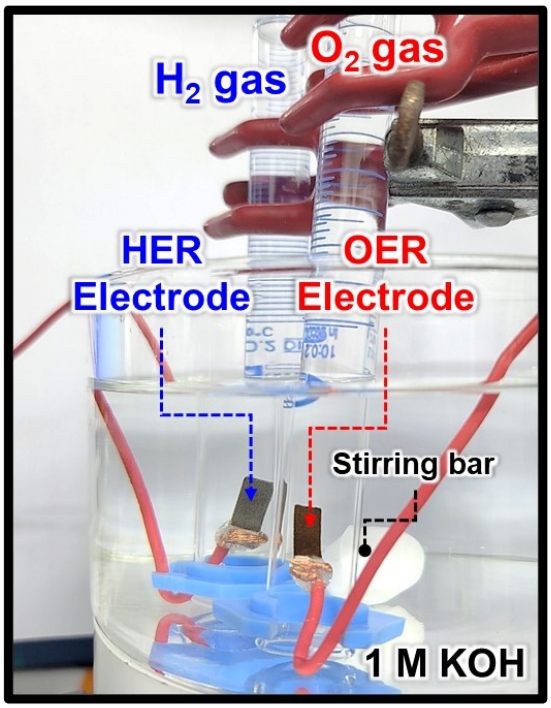

Fig. S39. The photograph image of experimental set-ups of water displacement for collection of the evolved gas.

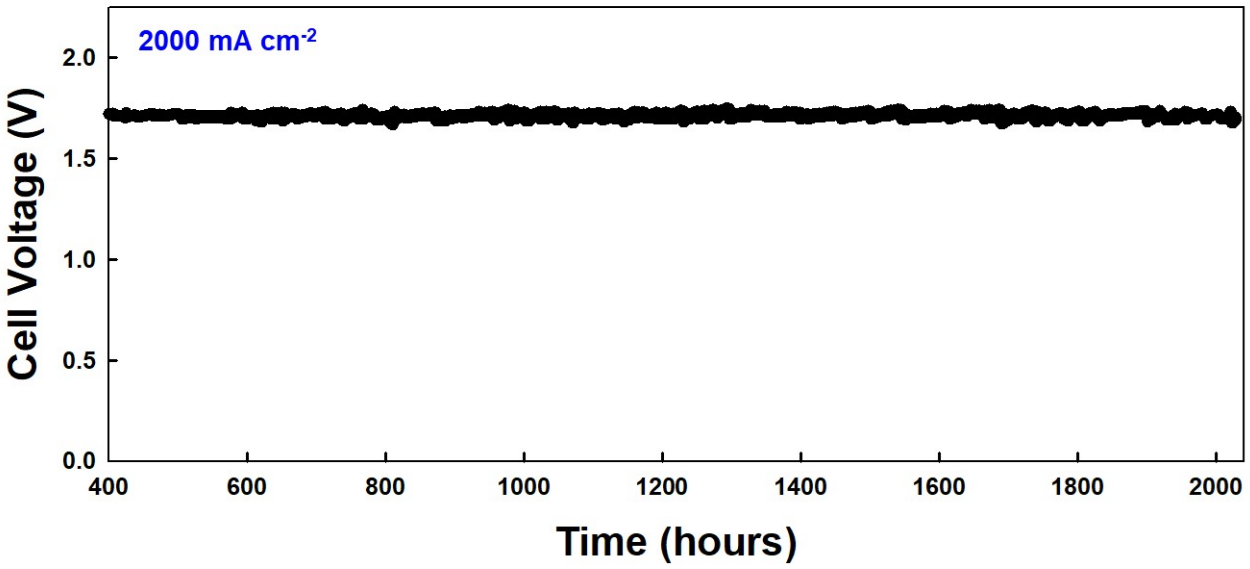

Fig. S40. Chronopotentiometry curve for EP Ni–CST ‖ EP NiFeCo–CST electrodes recorded at 2000 mA cm^{-2}.

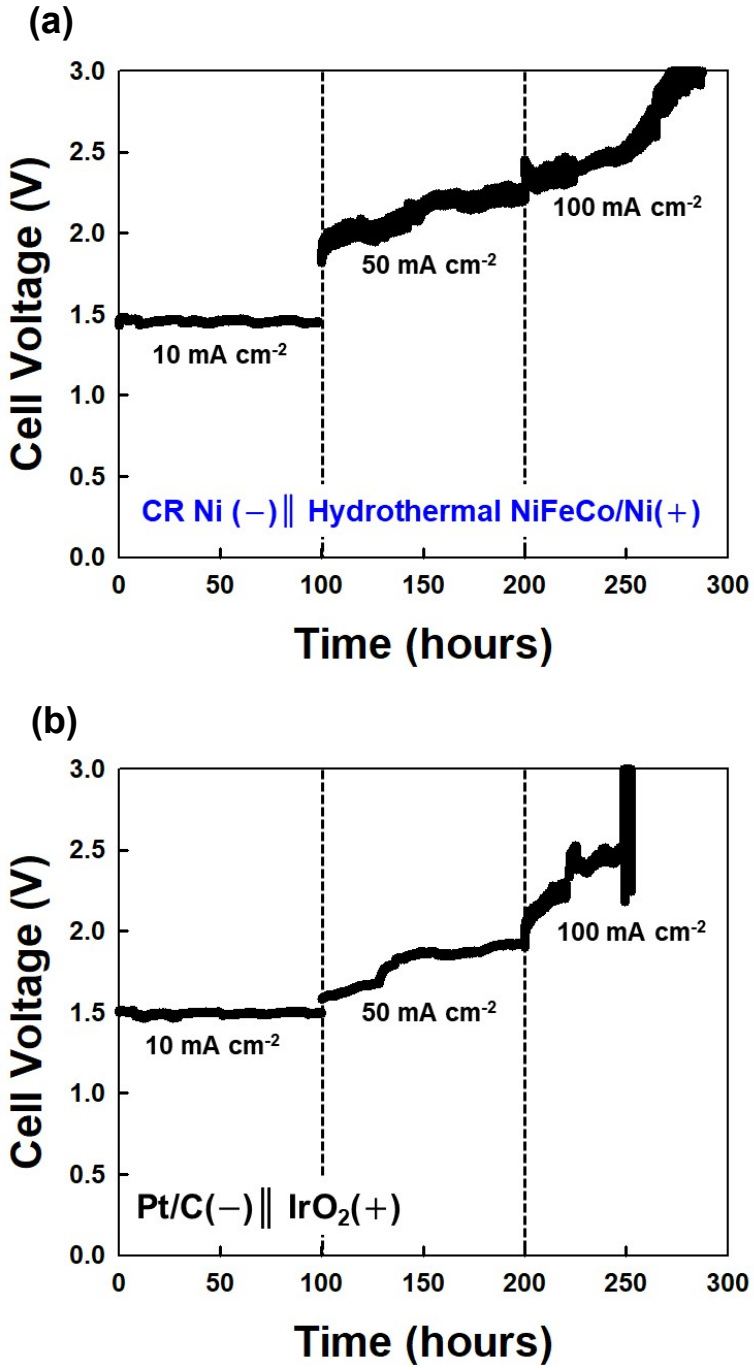

Fig. S41. Stability test of the electrodes. (a) Chronopotentiometry curve for CR Ni–CST ‖ Hydrothermal NiFeCo–CST cell, and (b) Pt/C/Ni foam ‖ IrO_2/Ni foam cell obtained at current density of 10, 50, and 100 mA cm^{-2}.

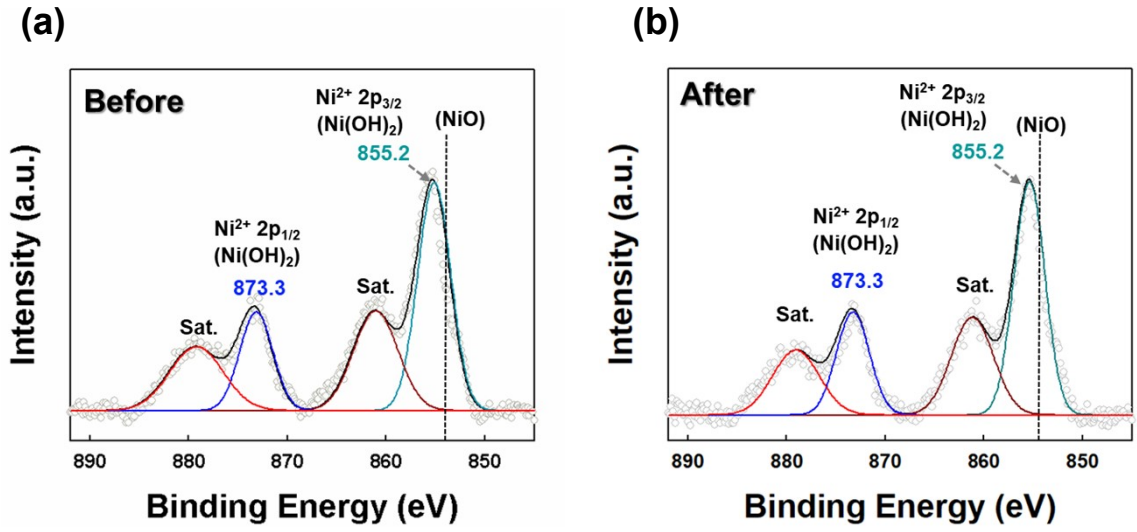

Fig. S42. Ni 2p XPS spectra of EP Ni–CST (a) before and (b) after stability test.

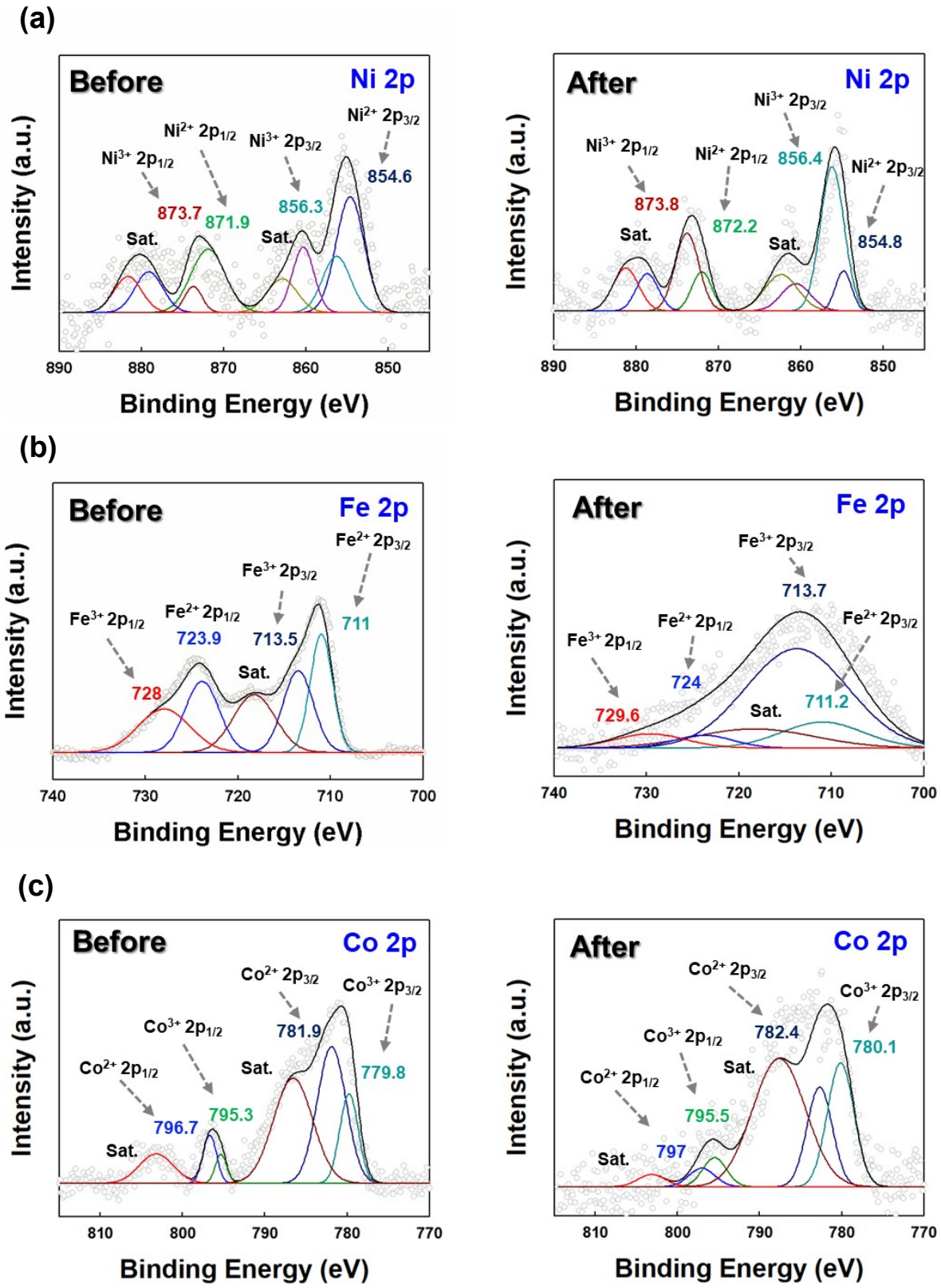

Fig. S43. (a) Ni 2p, (b) Fe 2p, and (c) Co 2p XPS spectra of EP NiFeCo–CST before and after stability test.[S24-S26]

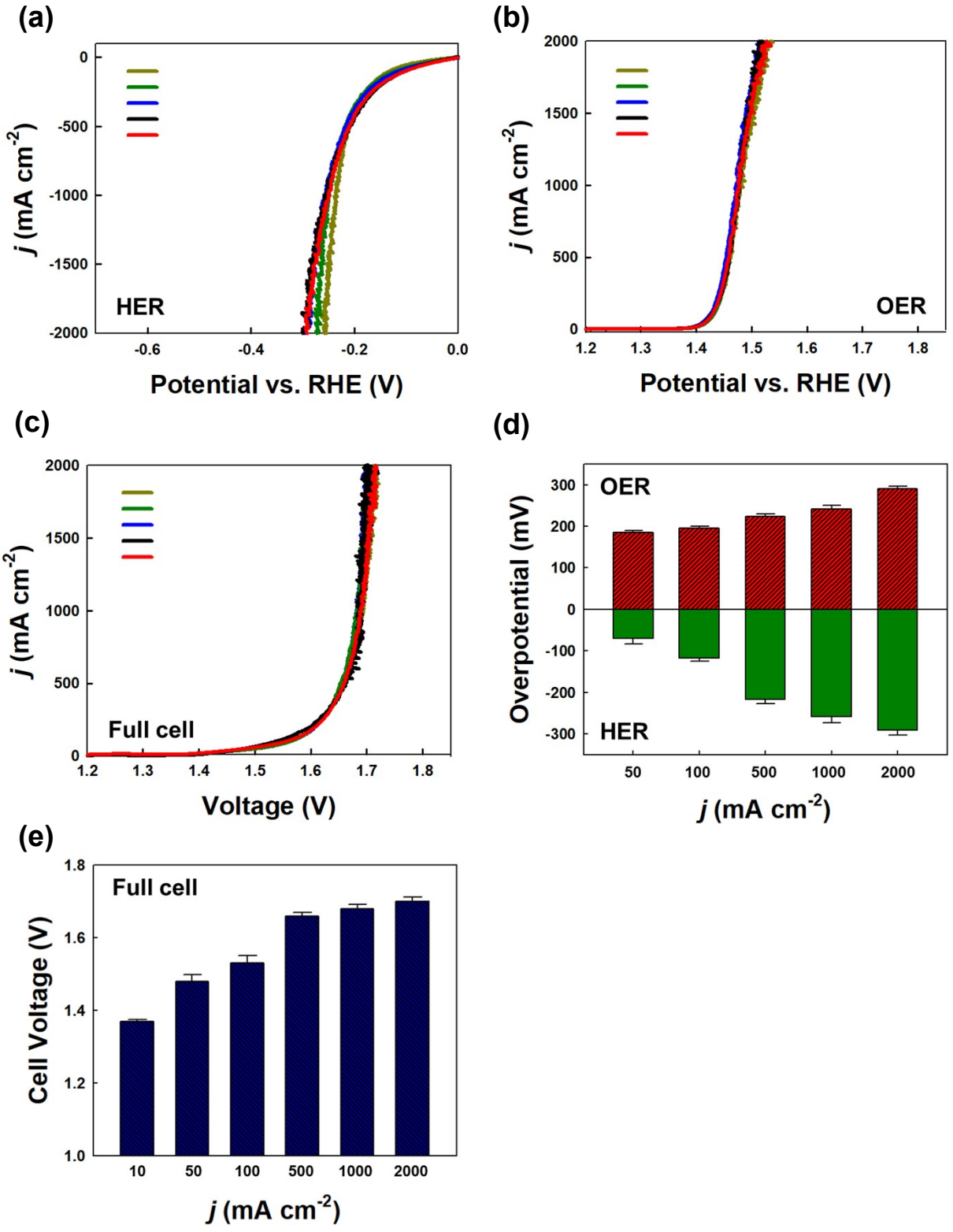

Fig. S44. Reproducibility of the (a) HER (EP Ni–CST electrodes), (b) OER (EP NiFeCo–CST electrodes), and (c) overall splitting (EP Ni–CST‖EP NiFeCo–CST electrodes) performance. (d) Overpotentials obtained from HER and OER polarization curves, and (e) cell voltages obtained from overall water-splitting polarization curves of our electrodes.

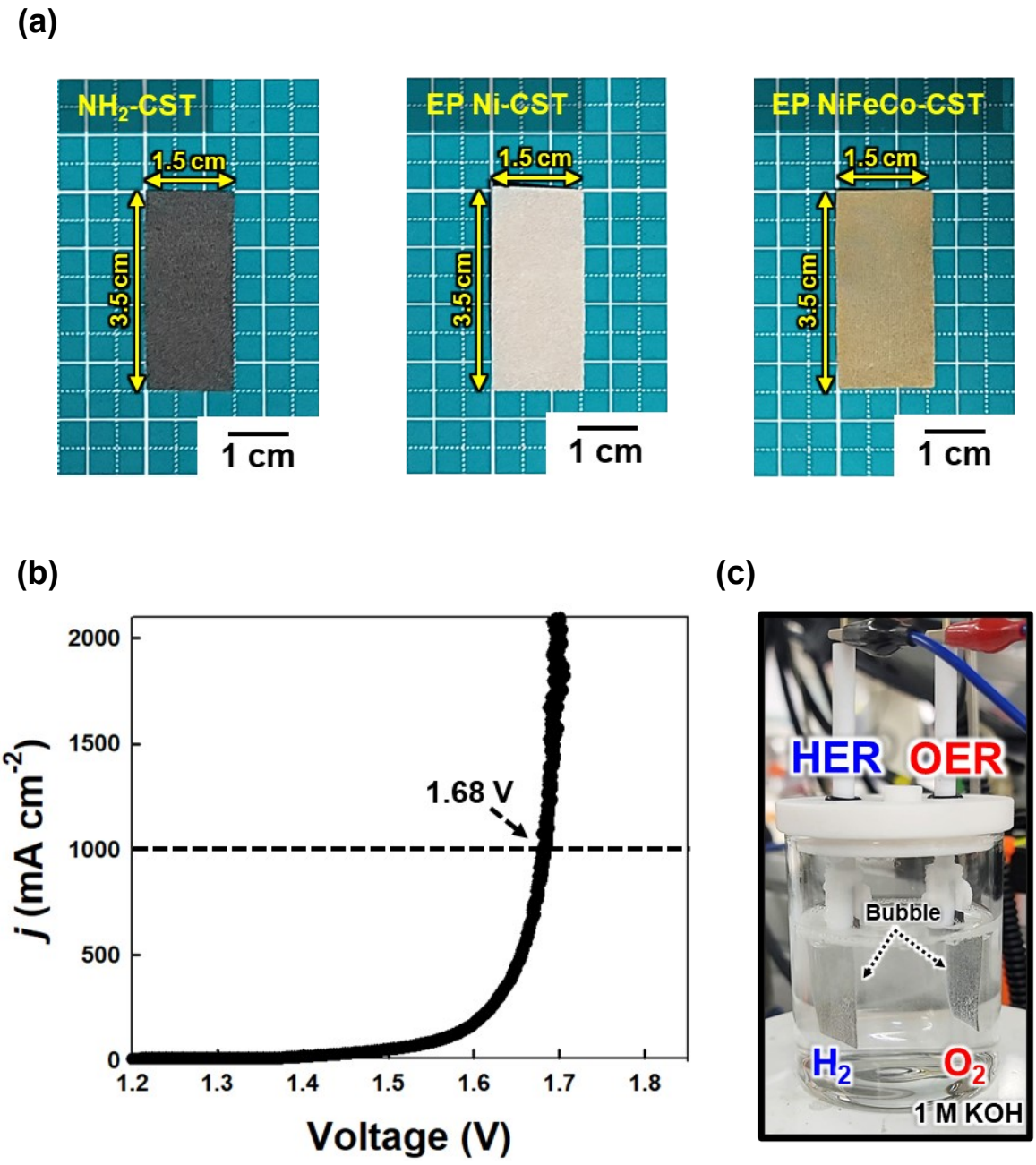

Fig. S45. (a) The photographic images of NH_2–CST, EP Ni–CST and EP NiFeCo–CST. (b) Polarization curves and (c) the photographic image of the EP Ni–CST ‖ EP NiFeCo–CST electrodes.

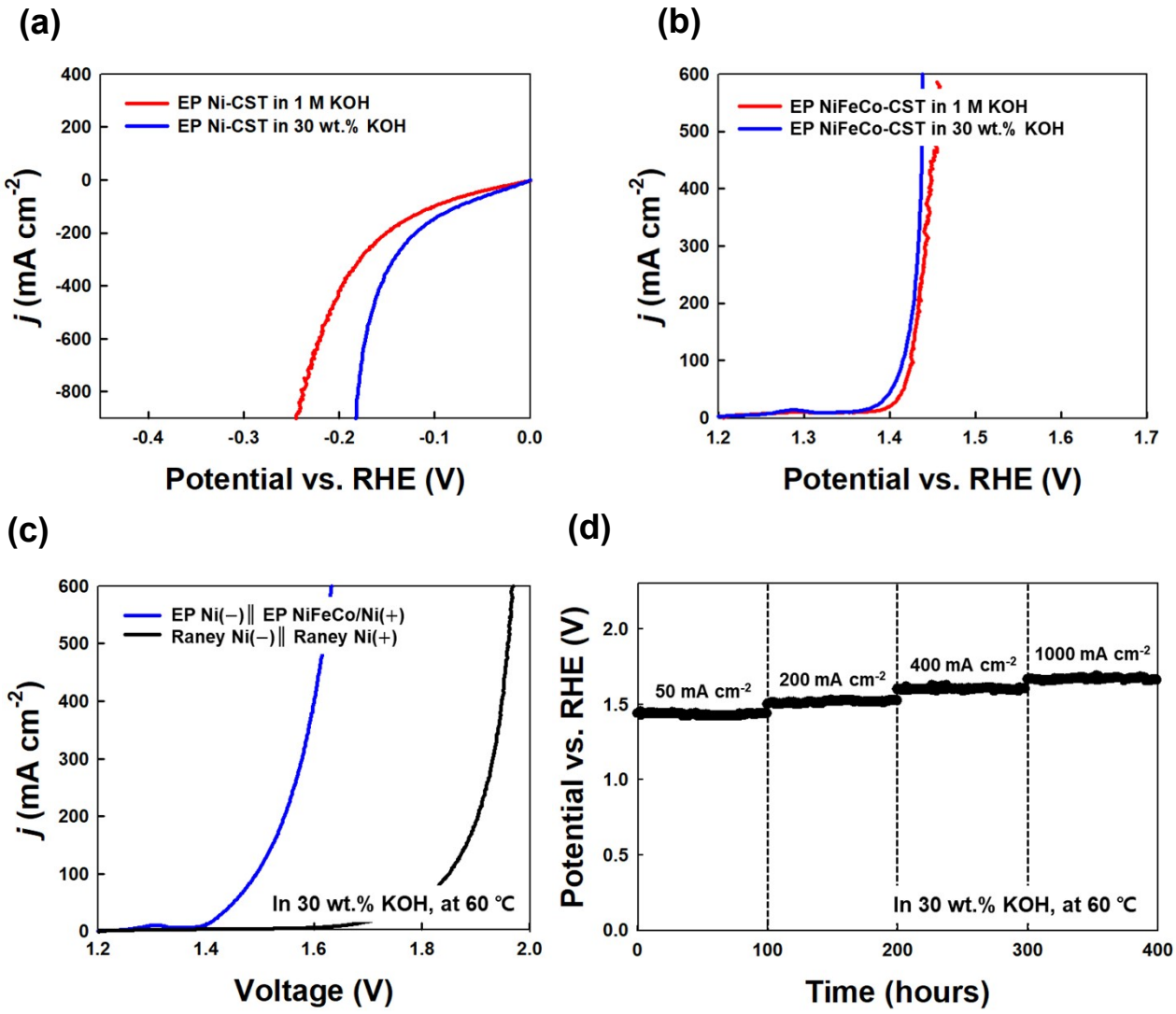

Fig. S46. (a) HER polarization curves of the EP Ni–CST electrodes. (b) OER polarization curves of the EP NiFeCo–CST electrodes. (c) Polarization curves of the EP Ni–CST‖EP NiFeCo–CST electrodes and conventional water-splitting electrodes (Raney nickel/Ni foam) measured in a 30 wt.% KOH electrolyte at 60 ℃. (d) Chronopotentiometry curves of the EP Ni–CST‖EP NiFeCo–CST electrodes (at 50, 200, 400, and 1,000 mA cm^{-2}) measured in a 30 wt.% KOH electrolyte at 60 ℃. In this case, Raney nickel/Ni foam electrodes were prepared by drop-casting and the catalyst loading amount was 0.84 mg cm^{-2}.

Table S1. Atomic composition ratio data of COOH–CST.

Atomic composition (%)		
	[a] CST	**COOH–CST**
C	90.2	**73.3**
O	6.9	**22.7**
N	2.5	3.6

[a] CST: Carbonized silk textile

Table S2. Performance comparison of Ni-based HER electrodes.

HER catalyst	Method	Overpotential (mV)	Tafel plot (mV dec^{-1})	Reference
EP Ni–CST	**Carbonization/ interfacial assembly-driven electroplating**	**12 @10 mA cm^{-2}**	**31.8**	**Our work**
Ni_5Co_3Mo-OH nanosheets/Ni foam	Chloride corrosion	52 @10 mA cm^{-2}	59	[S34]
Mo-Ni_3S_2/Ni_xP_y/Ni foam	Solvothermal	109 @10 mA cm^{-2} 128 @20 mA cm^{-2}	68.4	[S36]
Ni/$NiFeMoO_x$/Ni foam	Hydrothermal	22 @10 mA cm^{-2} 117 @100 mA cm^{-2}	76	[S39]
Ni_3N-VN/ commercial Ni foam	Hydrothermal	64 @10 mA cm^{-2} 218 @100 mA cm^{-2}	37	[S40]
Ni-Fe-MoN NTs	Hydrothermal	55 @10 mA cm^{-2} 199 @100 mA cm^{-2}	109	[S41]
Ni-Co-P HNBs [a)]	Microwave	107 @10 mA cm^{-2}	46	[S45]
Ni/Mo_2C-NCNFs [b)]	Electrospinning, carbonization	143 @10 mA cm^{-2}	57.8	[S48]
NiFeOx@NiCu	Solvothermal	66 @10 mA cm^{-2}	67.8	[S49]

a) HNBs : hollow nanobricks

b) NCNFs : nitrogen-doped carbon nanofibers

Table S3. Performance comparison of Ni-based OER electrodes.

OER catalyst	Method	Overpotential (mV)	Tafel plot (mV dec^{-1})	Reference
EP NiFeCo–CST	**Carbonization/ interfacial assembly-driven electroplating**	**186 @50 mA cm^{-2} 196 @100 mA cm^{-2}**	**30.9**	**Our work**
Ni_5Co_3Mo-OH nanosheets/Ni foam	Chloride corrosion	304 @100 mA cm^{-2}	56.4	[S34]
Ni_2P-CuP_2/CNT [a]/ Graphene/Ni foam	Chemical vapor deposition	190 @50 mA cm^{-2} 300 @100 mA cm^{-2}	42	[S35]
Mo-Ni_3S_2/Ni_xP_y/Ni foam	Solvothermal	238 @50 mA cm^{-2} 270 @100 mA cm^{-2}	60.6	[S36]
Ni/NiFeMoO_x/Ni foam	Hydrothermal	255 @10 mA cm^{-2} 289 @100 mA cm^{-2}	35	[S39]
Ni_2P-VP_2/ commercial Ni foam	Hydrothermal	306 @50 mA cm^{-2} 398 @100 mA cm^{-2}	49	[S40]
Ni-Fe-MoN NTs	Hydrothermal	228 @10 mA cm^{-2} 305 @100 mA cm^{-2}	41	[S41]
Ni-Co-P HNBs [b]	Microwave	270 @10 mA cm^{-2}	76	[S45]
Ni/Mo_2C-NCNFs [c]	Electrospinning, carbonization	288 @10 mA cm^{-2}	78.4	[S48]
Ni–Fe LDH@NiCu	Solvothermal	218 @10 mA cm^{-2}	56.9	[S49]

a) CNT : carbon nanotube

b) HNBs : hollow nanobricks

c) NCNFs : nitrogen-doped carbon nanofibers

Table S4. Performance comparison of Ni-based overall water splitting electrodes.

HER catalyst (Cathode)	OER catalyst (Anode)	Method	Voltage (V)	Reference
EP Ni–CST	**EP NiFeCo–CST**	**Carbonization/interfacial assembly-driven electroplating**	**1.37 @10 mA cm^{-2}**	**Our work**
FeP/Ni_2P	FeP/Ni_2P	Chemical vapor deposition	1.42 @10 mA cm^{-2}	[S22]
Ni_5Co_3Mo-OH nanosheets/Ni foam	Ni_5Co_3Mo-OH nanosheets/Ni foam	Chloride corrosion	1.43 @10 mA cm^{-2}	[S34]
Ni_2P-CuP_2/CNT [a)]/ Graphene/Ni foam	Ni_2P-CuP_2/CNT/ Graphene/Ni foam	Chemical vapor deposition	1.45 @10 mA cm^{-2}	[S35]
Mo-Ni_3S_2/Ni_xP_y/Ni foam	Mo-Ni_3S_2/Ni_xP_y/Ni foam	Solvothermal	1.46 @10 mA cm^{-2}	[S36]
N-Ni_3S_2/Ni foam	N-Ni_3S_2/Ni foam	Thiourea calcination	1.48 @10 mA cm^{-2}	[S37]
FeNi-MOF/Ni foam	FeNi-MOF/Ni foam	Solvothermal	1.495 @10 mA cm^{-2}	[S38]
Ni/NiFeMoO_x/Ni foam	Ni/NiFeMoO_x/Ni foam	Hydrothermal	1.5 @10 mA cm^{-2}	[S39]
Ni_3N-VN/ commercial Ni foam	Ni_2P-VP_2/ commercial Ni foam	Hydrothermal	1.51 @10 mA cm^{-2}	[S40]
Ni-Fe-MoN NTs	Ni-Fe-MoN NTs	Hydrothermal	1.513 @10 mA cm^{-2}	[S41]
Ni_2N-NiMoN/Carbon cloth	Ni_2N-NiMoN/ Carbon cloth	Hydrothermal	1.54 @10 mA cm^{-2}	[S42]
NiFe/Cu NW [b)]/Cu	NiFe/Cu NW/Cu	Electroplating	1.54 @10	[S43]

foam	foam		mA cm^{-2}	
$Ni_{11}(HPO_3)_8(OH)_6$ /Ni foam	$Ni_{11}(HPO_3)_8(OH)_6$ /Ni foam	Hydrothermal	1.6 @10 mA cm^{-2}	[S44]
Ni-Co-P HNBs [c]	Ni-Co-P HNBs	Microwave	1.62 @10 mA cm^{-2}	[S45]
$NiCo_2S_4$ NW/ Ni foam	$NiCo_2S_4$ NW/ Ni foam	Hydrothermal	1.63 @10 mA cm^{-2}	[S46]
Ni-Fe-O Nw [b]	Ni-Fe-O Nw	Chemical dealloying (NaOH)	1.64 @10 mA cm^{-2}	[S47]
Ni/Mo_2C-NCNFs [d]	Ni/Mo_2C-NCNFs	Electrospinning, carbonization	1.64 @10 mA cm^{-2}	[S48]

a) CNT : carbon nanotube

b) NW : nanowire

c) HNBs : hollow nanobricks

d) NCNFs : nitrogen-doped carbon nanofibers

Table S5. Durability comparison of Ni-based overall water splitting electrodes.

HER catalyst (Cathode)	OER catalyst (Anode)	Method	Current density (mA cm^{-2})	Durability (hour)	Reference
EP Ni–CST	**EP NiFeCo–CST**	**Carbonization/interfacial assembly-driven electroplating**	**2000**	**> at least 1640 h**	**Our work**
FeP/Ni_2P	FeP/Ni_2P	Chemical vapor deposition	500	40 h	[S22]
Ni_5Co_3Mo-OH nanosheets/ Ni foam	Ni_5Co_3Mo-OH nanosheets/ Ni foam	Chloride corrosion	100	100 h	[S34]
N-Ni_3S_2/Ni foam	N-Ni_3S_2/Ni foam	Thiourea calcination	20	8 h	[S37]
FeNi-MOF/Ni foam	FeNi-MOF/Ni foam	Solvothermal	500	100 h	[S38]
Ni/NiFeMoO_x/Ni foam	Ni/NiFeMoO_x/Ni foam	Hydrothermal	500	100 h	[S39]
Ni_3N-VN/ commercial Ni foam	Ni_2P-VP_2/ commercial Ni foam	Hydrothermal	10	100 h	[S40]
Ni-Fe-MoN NTs	Ni-Fe-MoN NTs	Hydrothermal	360	45 h	[S41]
Ni_2N-NiMoN/Carbon cloth	Ni_2N-NiMoN/ Carbon cloth	Hydrothermal	10	20 h	[S42]
NiFe/Cu NW [a)]/Cu foam	NiFe/Cu NW/Cu foam	Electroplating	100	24 h	[S43]
$Ni_{11}(HPO_3)_8(OH)_6$/Ni	$Ni_{11}(HPO_3)_8(OH)_6$/Ni	Hydrothermal	10	100 h	[S44]

foam	foam				
Ni-Co-P HNBs [b)]	Ni-Co-P HNBs	Microwave	10	20 h	[S45]
$NiCo_2S_4$ NW/ Ni foam	$NiCo_2S_4$ NW/ Ni foam	Hydrothermal	10	50 h	[S46]
Ni-Fe-O Nw	Ni-Fe-O Nw	Chemical dealloying (NaOH)	10	10 h	[S47]
Ni/Mo_2C-NCNFs [c)]	Ni/Mo_2C-NCNFs	Electrospinning, carbonization	10	100 h	[S48]

a) NW: nanowire

b) HNBs : hollow nanobricks

c) NCNFs : nitrogen-doped carbon nanofibers

Table S6. Ni, Fe, and Co atomic ratio of large area EP NiFeCo–CST electrode.

	Atomic ratio		
	1	**2**	**3**
Ni:Fe:Co	1:0.98:0.97	1:1.01:0.96	1:1.07:0.92

References

S1 O. P. Watts, *Trans. Am. Electrochem. Soc*., 1916, **29**, 395–403

S2 S.-S. Tzeng and F.-Y. Chang, *Thin Solid Films*, 2001, **388**, 143.

S3 X. Liu, X. Wang, X. Yuan, W. Donga and F. Huang, *J. Mater. Chem. A*, 2016, **4**, 167

S4 J. Yin, Y. Li, F. Lv, Q. Fan, Y-Q. Zhao, Q. Zhang, W. Wang, F. Cheng, P.Xi, and S. Guo, *ACS Nano*, 2017, **11**, 2275-2283

S5 S. Zhao, J. Huang, Y. Liu, J. Shen, H. Wang, X. Yang, Y. Zhu, and C. Li, *J. Mater. Chem. A*, 2017, **5**, 4207-4214

S6 S. J. Clark, M. D. Segall, C. J. Pickard, P. J. Hasnip, M. I. Probert, K. Refson and M. C. *Z.* Payne, *Kristallogr.,* 2005, **220**, 567-570.

S7 H. S. Ahn and A. J. Bard, *J. Am. Chem. Soc.,* 2015, **138**, 313-318.

S8 J. D. Michael, E. L. Demeter, S. M. Illes, Q. Fan, J. R. Boes and J. R. Kitchin, *J. Phys. Chem. C.,* 2015, **119**, 11475-11481.

S9 F. Malara, A. Minguzzi, M. Marelli, S. Morandi, R. Psaro, V. Dal Santo and A. Naldoni, *ACS Catal.,* 2015, **5**, 5292-5300.

S10 H. Zhang, J. Cheng, F. Lin, H. He, J. Mao, K. S. Wong and W. C. Choy, *ACS Nano,* 2015, **10**, 1503-1511.

S11 F. Costanzo, *Phys. Chem. Chem. Phys.,* 2016, **18**, 7490-7501.

S12 M. García-Mota, M. Bajdich, V. Viswanathan, A. Vojvodic, A. T. Bell and J. K. Nørskov, *J. Phys. Chem. C*, 2012, **116**, 21077-21082.

S13 M. Bajdich, M. García-Mota, A. Vojvodic, J. K. Nørskov and A. T. Bell, *J. Am. Chem. Soc.,* 2013, **135**, 13521-13530.

S14 D. Friebel, M. W. Louie, M. Bajdich, K. E. Sanwald, Y. Cai, A. M. Wise and R. C. Davis, *J. Am. Chem. Soc.,* 2015, **137**, 1305.

S15 Y. F. Li and A. Selloni, *ACS Catal.,* 2014, **4**, 1148.

S16 Q. Liang, G. Brocks and A. Bieberle-Hutter, *J. Phys. Energy*, 2021, **3**, 26001.

S17 A. S. Rajan, S. Sampath and A. K. Shukla, *Energy Environ. Sci.,* 2014, **7**, 1110-1116.

S18 S. H. Lim, R. Li, W. Ji and J. Lin, *Phys. Rev. B*, 2007, **76**, 195406.

S19 Z. Zhu, H. Yin, C.-T. He, M. Al-Mamun, P. Liu, L. Jiang, Y. Zhao, Y. Wang, H.-G. Yang, Z. Tang, D. Wang, X.-M. Chen and H. Zhao, *Adv. Mater.,* 2018, **30**, 1801171.

S20 S. Sun, P. Diao, C. Feng, E.-M. Ungureanu, Y. Tang, B. Hu and Q. Hu, *RSC Adv*., 2018, **8**, 19776-19785.

S21 B. Zhang, L. Zhang, Q. Tan, J. Wang, J. Liu, H. Wan, L. Miao and J. Jiang, *Energy Environ. Sci.*, 2020, **13**, 3007-3013.

S22 F. Yu, H. Zhou, Y. Huang, J. Sun, F. Qin, J. Bao, W. A. Goddard, S. Chen and Z. Ren, *Nat. Commun*., 2018, **9**, 2551.

S23 J. Rossmeisl, Z. W. Qu, H. Zhu, G. J. Kroes and J. K. Nørskov, *J. Electroanal. Chem.*, 2007, **607**, 83-89.

S24 C. Xiao, Y. Li, X. Lu and C. Zhao, *Adv. Funct. Mater.,* 2016, **26**, 3515-3523.

S25 Y. Tang, X. Li, H. Lv, D. Xie, W. Wang, C. Zhi and H. Li, *Adv. Energy Mater.,* 2020, **10**, 2000892.

S26 J. Wang, R. Gao, D. Zhou, Z. Chen, Z. Wu, G. Schumacher, Z. Hu and X. Liu, *ACS Catal.,* 2017, **7**, 6533-6541.

S27 J. Duan, S. Chen, A. Vasileff and S. Z. Qiao, *ACS Nano*, 2016, **10**, 8738-8745.

S28 X. Luo, X. Wei, H. Zhong, H. Wang, Y. Wu, Q. Wang, W. Gu, M. Gu, S. P. Beckman and C. Zhu, *ACS Appl. Mater. Interfaces*, 2020, **12**, 3539-3546.

S29 M. Zhang, Y. Liu, B. Liu, Z. Chen, H. Xu and K. Yan, *ACS Catal*., 2020, **10**, 5179-5189.

S30 M. Görlin, P. Chernev, J. Ferreira de Araújo, T. Reier, S. Dresp, B. Paul, R. Krähnert, H. Dau and P. Strasser, *J. Am. Chem. Soc.*, 2016, **138**, 5603-5614.

S31 A. Moysiadou, S. Lee, C.-S. Hsu, H. M. Chen and X. Hu, *J. Am. Chem. Soc.*, 2020, **142**, 11901-11914.

S32 F. Dionigi, Z. Zeng, I. Sinev, T. Merzdorf, S. Deshpande, M. B. Lopez, S. Kunze, I. Zegkinoglou, H. Sarodnik, D. Fan, A. Bergmann, J. Drnec, J. F. d. Araujo, M. Gliech, D. Teschner, J. Zhu, W.-X. Li, J. Greeley, B. R. Cuenya and P. Strasser, *Nat. Commun*., 2020, **11**, 2522.

S33 R. D. L. Smith, C. Pasquini, S. Loos, P. Chernev, K. Klingan, P. Kubella, M. R. Mohammadi, D. Gonzalez-Flores and H. Dau, *Nat. Commun*., 2017, **8**, 2022.

S34 S. Hao, L. Chen, C. Yu, B. Yang, Z. Li, Y. Hou, L. Lei and X. Zhang, *ACS Energy Lett.*, 2019, **4**, 952-959.

S35 S. Riyajuddin, K. Azmi, M. Pahuja, S. Kumar, T. Maruyama, C. Bera and K. Ghosh, *ACS Nano*, 2021, **15**, 5586-5599.

S36 X. Luo, P. Ji, P. Wang, R. Cheng, D. Chen, C. Lin, J. Zhang, J. He, Z. Shi, N. Li, S. Xiao and S. Mu, *Adv. Energy. Mater.*, 2020, **10**, 1903891.

S37 P. Chen, T. Zhou, M. Zhang, Y. Tong, C. Zhong, N. Zhang, L. Zhang, C. Wu and Y. Xie, *Adv. Mater.* 2017, **29,** 1701584.

S38 D. Senthil Raja, H.-W. Lin and S.-Y. Lu, *Nano Energy* 2019, **57**, 1.

S39 Y.-K Li, G. Zhang, W.-T. Lu and F.-F Cao, *Adv. Sci.*, 2020, **7**, 1902034.

S40 H. Yan, Y. Xie, A. Wu, Z.Cai, L. Wang, C. Tian, X. Zhang and H. Fu, *Adv. Mater.,* 2019, **31**, 1901174.

S41 C. Zhu, Z. Yin, W. Lai, Y. Sun, L. Liu, X. Zhang, Y. Chen and S.-L. Chou, *Adv. Energy. Mater.*, 2018, **8**, 1802327.

S42 A. Wu, Y. Xie, H. Ma, C. Tian, Y. Gu, H. Yan, X. Zhang, G. Yang and H. Fu, *Nano Energy* 2018, **44**, 353.

S43 L. Yu, H. Zhou, J. Sun, F. Qin, F. Yu, J. Bao, Y. Yu, S. Chen and Z. Ren, *Energy Environ. Sci*., 2017, **10**, 1820.

S44 P. W. Menezes, C. Panda, S. Loos, F. Bunschei-Bruns, C. Walter, M. Schwarze, X. Deng, H. Dau and M. Driess, *Energy Environ. Sci*., 2018, **11**, 1287.

S45 E. Hu, Y. Feng, J. Nai, D. Zhao, Y. Hu and X. W. Lou, *Energy Environ. Sci.*, 2018, **11**, 872-880.

S46 A. Sivanantham, P. Ganesan and S. Shanmugam, *Adv. Funct. Mater.,* 2016, **26**, 4661.

S47 C. Dong, T. Kou, H. Gao, Z. Peng and Z. Zhang, *Adv. Energy. Mater.*, 2018, **8**, 1701347.

S48 M. Li, Y. Zhu, H. Wang, C.Wang, N. Pinna and X. Lu, *Adv. Energy. Mater.*, 2019, **9**, 1803185.

S49 Y. Zhou, Z. Wang, Z. Pan, L. Liu, J. Xi, X. Luo and Y. Shen, *Adv. Mater.,* 2019, **31**, 1806769.